nature biotechnology

ARTICLES

https://doi.org/10.1038/s41587-021-01074-4

A fluorescent sensor for spatiotemporally resolved imaging of endocannabinoid dynamics in vivo

Ao Dong[1,2,3], Kaikai He[1,2], Barna Dudok[4], Jordan S. Farrell[4], Wuqiang Guan[5], Daniel J. Liput[6,7], Henry L. Puhl[7], Ruyi Cai[1,2], Huan Wang[1,2], Jiali Duan[1,2], Eddy Albarran[8], Jun Ding[9], David M. Lovinger[6], Bo Li[5], Ivan Soltesz[4] and Yulong Li[1,2,3,10] ✉

Endocannabinoids (eCBs) are retrograde neuromodulators with important functions in a wide range of physiological processes, but their in vivo dynamics remain largely uncharacterized. Here we developed a genetically encoded eCB sensor called $GRAB_{eCB2.0}$. $GRAB_{eCB2.0}$ consists of a circular-permutated EGFP and the human CB1 cannabinoid receptor, providing cell membrane trafficking, second-resolution kinetics with high specificity for eCBs, and shows a robust fluorescence response at physiological eCB concentrations. Using $GRAB_{eCB2.0}$, we monitored evoked and spontaneous changes in eCB dynamics in cultured neurons and acute brain slices. We observed spontaneous compartmentalized eCB transients in cultured neurons and eCB transients from single axonal boutons in acute brain slices, suggesting constrained, localized eCB signaling. When $GRAB_{eCB2.0}$ was expressed in the mouse brain, we observed foot shock-elicited and running-triggered eCB signaling in the basolateral amygdala and hippocampus, respectively. In a mouse model of epilepsy, we observed a spreading wave of eCB release that followed a Ca^{2+} wave through the hippocampus. $GRAB_{eCB2.0}$ is a robust probe for eCB release in vivo.

Cannabis derivatives have long been used for medicinal and recreational purposes across cultures[1]. Bioactive compounds in cannabis, phytocannabinoids, exert their function by 'hijacking' the body's endogenous cannabinoid (eCB) system. The biological function of eCBs (mainly two lipid metabolites, 2-arachidonoylglycerol (2-AG) and anandamide (AEA)) is primarily mediated by the activation of type 1 and type 2 cannabinoid receptors (CB1R and CB2R)[2]. eCBs are widely distributed throughout the peripheral and central nervous system, where they serve as important neuromodulators. Interestingly, unlike other classical neurotransmitters stored in synaptic vesicles and released from the presynaptic terminal, eCBs are typically produced and released from the postsynaptic compartment in a neuronal activity-dependent manner and then retrogradely travel to the presynaptic terminal and activate the CB1R, which often results in an inhibition of presynaptic neurotransmitter release[3,4]. In addition, eCBs also play a role in glial cells and in intracellular organelles[5–9]. In the brain, eCBs participate in short-term and long-term synaptic plasticity of glutamatergic and γ-aminobutyric acid (GABA)ergic synapses in a variety of regions, including the cerebral cortex, hippocampus, striatum, ventral tegmental area, amygdala and cerebellum[4,10], playing important roles in a wide range of physiological processes such as development, emotional state, pain, the sleep–wake cycle, energy metabolism, reward and learning and memory[11–15]. Given the broad distribution and variety of functions of eCBs, dysregulation of the eCB system has been associated with a plethora of disorders, including neuropsychiatric and neurodegenerative diseases, epilepsy, cancer and others[16–18]. The eCB system has therefore emerged as a promising target for treating neurological diseases[19,20].

Although we know much about eCB biochemistry and physiology, spatiotemporal dynamics of eCB release in the brain remain largely unknown. Signaling via eCB receptors is believed to last on the order of seconds and occurs over a distance on the order of tens of micrometers[21]. However, this assumption has not been tested definitively, largely because existing methods for measuring eCB signaling lack the necessary spatiotemporal resolution. For example, although qualitative and quantitative measurement of eCBs in brain tissues can provide valuable information regarding eCB levels, these measurements usually require extraction, purification and analysis of lipids by chromatography and mass spectrometry[22,23]; therefore, this approach has poor spatial and temporal resolution and cannot be used to measure eCBs in vivo. Another approach is electrophysiology coupled with pharmacology and/or genetics, which is often used to indirectly measure eCB activity by measuring eCB-mediated synaptic modulation[21,24–26]; however, this method is mostly used in in vitro preparations and has relatively low spatial resolution. Microdialysis, while challenging for hydrophobic lipid molecules, has been used to monitor eCB abundance in the brain during pharmacological manipulations and behaviors[27,28], but it has a long sampling interval (at least 5 min) that is well beyond the time scale of synaptic plasticity mediated by eCBs (approximately subseconds to seconds), preventing accurate detection of eCBs in real

[1]State Key Laboratory of Membrane Biology, Peking University School of Life Sciences, Beijing, China. [2]PKU-IDG/McGovern Institute for Brain Research, Beijing, China. [3]Peking-Tsinghua Center for Life Sciences, Academy for Advanced Interdisciplinary Studies, Peking University, Beijing, China. [4]Department of Neurosurgery, Stanford University, Palo Alto, CA, USA. [5]Cold Spring Harbor Laboratory, Cold Spring Harbor, NY, USA. [6]Laboratory for Integrative Neuroscience, National Institute on Alcohol Abuse and Alcoholism, Bethesda, MD, USA. [7]Laboratory of Molecular Physiology, National Institute on Alcohol Abuse and Alcoholism, Bethesda, MD, USA. [8]Neuroscience PhD Program, Stanford University, Palo Alto, CA, USA. [9]Department of Neurosurgery, Department of Neurology, Stanford University School of Medicine, Palo Alto, CA, USA. [10]Chinese Institute for Brain Research, Beijing, China. ✉e-mail: yulongli@pku.edu.cn

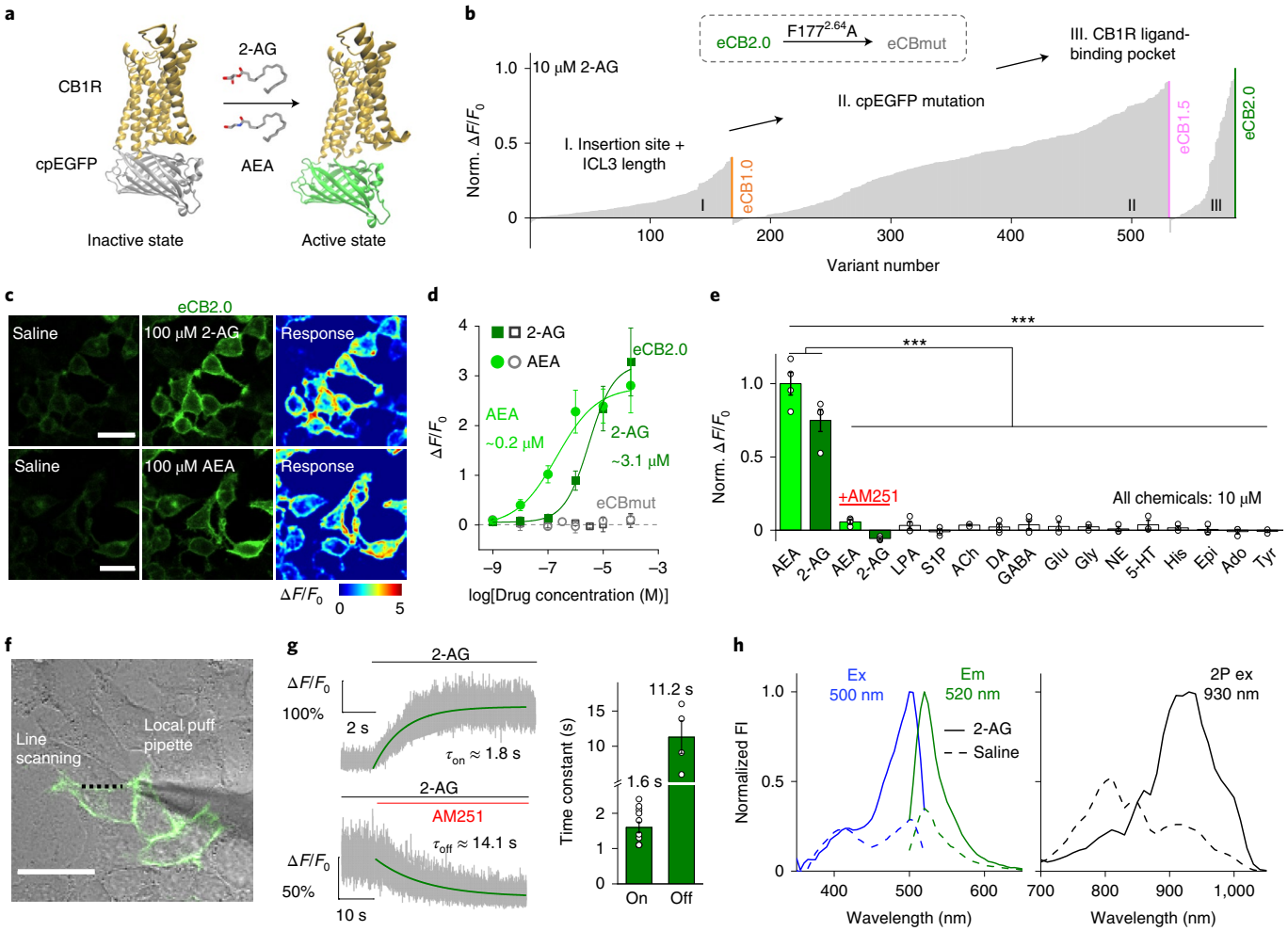

Fig. 1 | Development, optimization and characterization of GRAB$_{eCB}$ sensors in HEK293T cells. a, Schematic diagram depicting the design and principle of the GRAB$_{eCB}$ sensor, consisting of the CB1R and cpGFP. Ligand binding activates the sensor, inducing a change in fluorescence. **b**, Screening and optimization steps of GRAB$_{eCB}$ sensors and the normalized (norm.) fluorescence response to 10 μM 2-AG. **c**, Expression and fluorescence change in response to 100 μM 2-AG and AEA in HEK293T cells expressing eCB2.0. Similar results were observed for more than 20 cells. Scale bars, 30 μm. **d**, Dose–response curves measured in HEK293T cells expressing eCB2.0 or eCBmut, with the corresponding EC_{50} values for 2-AG and AEA shown; $n = 6$ experiments, mean ± s.e.m. **e**, Normalized fluorescence change in response to the indicated compounds (each at 10 μM) measured in cells expressing eCB2.0. When indicated, the CB1R inverse agonist AM251 was also added. LPA, lysophosphatidic acid; S1P, sphingosine-1-phosphate; ACh, acetylcholine; DA, dopamine; Glu, glutamate; Gly, glycine; NE, norepinephrine; 5-HT, 5-hydroxytryptamine; His, histamine; Epi, epinephrine; Ado, adenosine; Tyr, tyramine; $n = 3$ wells for ACh, Glu, Gly, NE, 5-HT, His, Epi, Ado and Tyr; $n = 4$ for other groups; mean ± s.e.m. A one-way ANOVA test was performed for all groups ($P = 8.00 \times 10^{-26}$); Tukey tests were performed post hoc ($P = 0$ (between 2-AG and AEA + AM251, 2-AG + AM251, LPA, … or Tyr), $P = 0$ (between AEA and AEA + AM251, 2-AG + AM251, LPA, … or Tyr)). **f**, Illustration of the localized puffing system using a glass pipette containing 100 μM 2-AG and/or AM251 positioned above an eCB2.0-expressing cell. The dotted black line indicates the ROI for line scanning. Similar results were observed for more than ten cells. Scale bar, 30 μm. **g**, Changes in eCB2.0 fluorescence were measured in an eCB2.0-expressing cell using line scanning; when indicated, 2-AG and AM251 were puffed onto the cell. The graph at the right summarizes on and off time constants measured upon application of 2-AG and upon application of AM251, respectively; $n = 11$ (τ_{on}) and $n = 4$ (τ_{off}) cells, mean ± s.e.m. **h**, One-photon excitation (ex) and emission (em) spectra and 2P excitation spectra of eCB2.0 in the absence and presence of 2-AG. Excitation and emission peaks are labeled. FI, fluorescence intensity. ***$P < 0.001$.

time in vivo. Therefore, development of an in vivo eCB-detection tool with satisfactory spatiotemporal resolution would meet a clear need in this field.

Recently, we and others developed a series of genetically encoded tools for sensing neurotransmitters and neuromodulators based on G protein-coupled receptors (GPCRs) and circular-permutated (cp) fluorescent proteins[29–37]. Using this highly successful strategy, we developed a new GPCR activation-based (GRAB) eCB sensor called GRAB$_{eCB2.0}$ (or simply eCB2.0) based on the human CB1R and cpEGFP. The eCB2.0 sensor has high specificity for eCBs, kinetics on the order of seconds and a fluorescence response of approximately 950% to 2-AG and 500% to AEA, respectively. After validating the in vitro performance of eCB2.0 in both cultured cells and acute brain slices, we then expressed the sensor in mice and reliably monitored foot shock-evoked eCB signals in the basolateral amygdala (BLA) in freely moving mice and eCB dynamics in the mouse hippocampus during running and seizure activity.

Results

Development and in vitro characterization of GRAB$_{eCB}$ sensors. Among the two eCB receptors, we chose CB1R as the scaffold for developing a GRAB eCB sensor, because this receptor has a higher

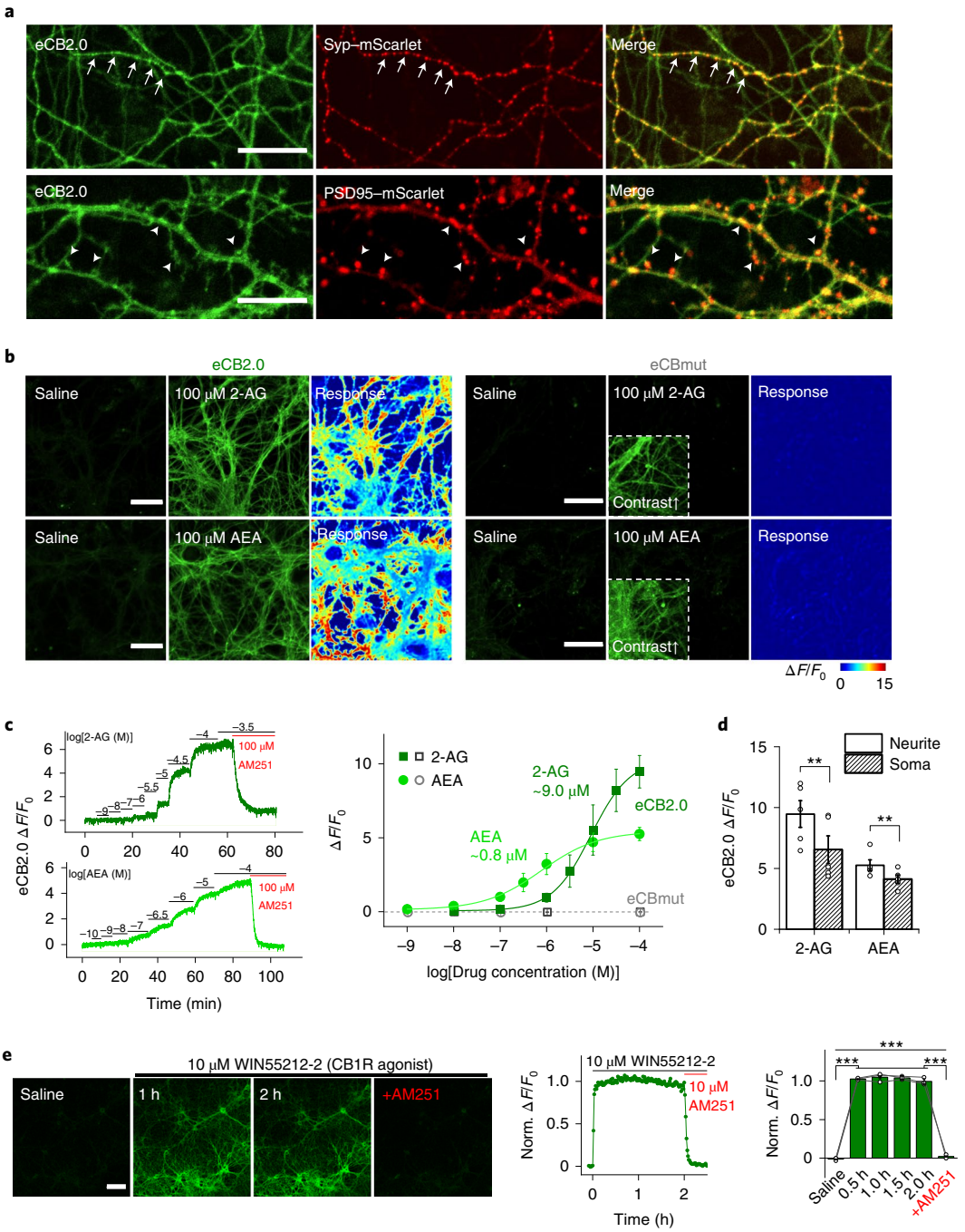

Fig. 2 | Characterization of GRAB$_{eCB}$ sensors in primary cultured neurons. a, Fluorescence microscopy images of primary cultured rat cortical neurons expressing eCB2.0 (green) and either synaptophysin (syp)–mScarlet (top row, red) or PSD95–mScarlet (bottom row, red). In the top row, arrows indicate axons; in the bottom row, arrowheads indicate dendrites and dendritic spines. Similar results were observed for more than ten neurons. Scale bars, 30 μm (top row) and 15 μm (bottom row). **b**, Fluorescence microscopy images and fluorescence response to 100 μM 2-AG (top row) or AEA (bottom row) in neurons expressing eCB2.0 (left) or eCBmut (right). Insets in eCBmut images are contrast enhanced to show expression of the sensor. Similar results were observed for more than 30 neurons. Scale bars, 30 μm. **c**, Left: example traces of $\Delta F/F_0$ measured in an eCB2.0-expressing neuron; the indicated concentrations of 2-AG and AEA, followed by 100 μM AM251, were applied. Right: dose–response curves measured in neurons expressing eCB2.0 or eCBmut, with the corresponding EC_{50} values shown; $n = 5$ cultures each, mean ± s.e.m. **d**, Summary of the change in eCB2.0 fluorescence in response to 100 μM 2-AG or AEA measured in neurites and soma; $n = 5$ cultures each, mean ± s.e.m. Paired two-tailed Student's *t*-tests were performed ($P = 0.0073$ (left) and 0.0068 (right)). **e**, Example images (left), trace (middle) and quantification (right) of the change in eCB2.0 fluorescence in response to a 2-h application of WIN55212-2, followed by AM251; $n = 3$ cultures each, mean ± s.e.m. Similar results were observed for more than 20 neurons. Scale bar, 100 μm. A one-way ANOVA test was performed for all groups ($P = 4.48 \times 10^{-13}$); Tukey tests were performed post hoc ($P = 0$ (between saline and 0.5 h, 1.0 h, 1.5 h or 2.0 h), $P = 0$ (between AM251 and 0.5 h, 1.0 h, 1.5 h or 2.0 h)). ***$P < 0.001$, **$P < 0.01$.

affinity for eCBs than CB2R[38]. We first inserted the intracellular loop 3 (ICL3)-cpEGFP module of our recently developed $GRAB_{NE}$ sensor[32] into the corresponding ICL3 in the human CB1R (Fig. 1a). After screening several insertion sites, we generated the prototype eCB sensor named $GRAB_{eCB0.1}$ (eCB0.1) with 30% fluorescent response to 10 μM 2-AG (Extended Data Fig. 1a). We speculated that the long ICL3 from $GRAB_{NE}$ may resist conformational coupling between CB1R and cpEGFP; therefore, we truncated the ICL3 of eCB0.1 and generated $GRAB_{eCB1.0}$ (eCB1.0) with 100% response to 2-AG (Fig. 1b and Extended Data Fig. 1a). To improve the dynamic range of our eCB sensor, we then selected eight residues in cpEGFP for individual randomized mutation based our experience gained through the development of previous GRAB sensors[29,31–33,35–37] (Extended Data Fig. 1a). Combining several single-mutation candidates, each with improved performance, resulted in the $GRAB_{eCB1.5}$ sensor (eCB1.5), which has a twofold higher response than eCB1.0 (Fig. 1b and Extended Data Fig. 1a). We next focused on the receptor's ligand-binding pocket to further improve the sensor's dynamic range and affinity. Residues $F177^{2.64}$, $V196^{3.32}$ and $S383^{7.39}$ were selected for targeted screening based on studies of CB1R structure[39–44] (Extended Data Fig. 1a). Interestingly, we found that introducing the $S383^{7.39}$T substitution into eCB1.5 produced an increased response to 2-AG, whereas the $F177^{2.64}$A substitution abolished the response to 2-AG (Extended Data Fig. 1a). We therefore selected the eCB1.5 with the $S383^{7.39}$T substitution as the second-generation $GRAB_{eCB2.0}$ sensor (eCB2.0) and eCB1.5 with both $S383^{7.39}$T and $F177^{2.64}$A substitutions as a non-responsive negative control, which we call the $GRAB_{eCBmut}$ sensor (eCBmut) (Fig. 1b and Extended Data Fig. 1b,c).

When expressed in HEK293T cells, both eCB2.0 and eCBmut sensors trafficked to the cell membrane (Fig. 1c). Upon ligand application of both 2-AG and AEA, eCB2.0 had concentration-dependent fluorescence increases, with a maximum response of approximately threefold relative to baseline and half-maximal effective concentrations (EC_{50}) for 2-AG and AEA of 3.1 μM and 0.2 μM, respectively; by contrast, eCBmut did not respond to 2-AG or AEA at any concentration tested (Fig. 1d). We then tested whether the sensor's response was specific to eCBs compared to other neurotransmitters. We found that eCB2.0 responded robustly to both 10 μM AEA and 2-AG, and the response was abolished by the CB1R inverse agonist AM251; moreover, no other tested neurotransmitters or neuromodulators elicited any response in cells expressing eCB2.0 (Fig. 1e). In addition, eCB2.0 responded robustly to synthetic CB1R agonists WIN55212-2 and CP55940 but weakly to the CB1R partial agonist Δ-9-THC (Extended Data Fig. 2).

Next, we measured the kinetics of eCB2.0 signaling using a rapid localized solution-application system in which compounds were puffed directly onto the cell (Fig. 1f). To measure the onset rate (τ_{on}), 100 μM 2-AG was puffed onto an eCB2.0-expressing cell; to measure the offset rate (τ_{off}), 100 μM AM251 was puffed onto a cell in the presence of 10 μM 2-AG. Using this approach, we measured average τ_{on} and τ_{off} values of 1.6 s and 11.2 s, respectively (Fig. 1g). To characterize photophysical properties of eCB2.0, we measured the fluorescent spectrum and photostability of eCB2.0 under one-photon (1P) and two-photon (2P) conditions. Peak 1P excitation (500-nm) and emission (520-nm) wavelengths as well as the peak 2P excitation (930-nm) wavelength of eCB2.0 were comparable to those of other common green fluorescent probes (Fig. 1h). In addition, eCB2.0 showed better photostability than EGFP under strong 1P illumination (Extended Data Fig. 3a–c) and better or comparable photostability than EGFP under 2P illumination (Extended Data Fig. 3d,e).

To examine whether eCB sensors couple with intracellular signaling pathways, we measured G protein activation using two approaches. First, we used a chimeric $G\alpha_{q-i}$ protein, which can be activated by G_i-coupled GPCR and can increase intracellular Ca^{2+} levels through phospholipase C (PLC) and inositol trisphosphate (IP3). jRGECO1a, a genetically encoded red calcium indicator, was also used to monitor intracellular Ca^{2+} signals (Extended Data Fig. 3f). In wild-type CB1R-expressing cells, 2-AG increased the fluorescent response of jRGECO1a in a dose-dependent manner, indicating that 2-AG successfully activated CB1R and the downstream G protein pathway; by contrast, 2-AG failed to induce a response from jRGECO1a in eCB2.0-expressing cells, demonstrating a lack of detectable coupling between eCB2.0 and G protein (Extended Data Fig. 3g,h). In addition, we found no significant difference in 2-AG-induced jRGECO1a signals between CB1R-expressing cells and CB1R- and eCB2.0-coexpressing cells, suggesting that the expression of eCB2.0 had a minimal buffering

Fig. 3 | Release of endogenous eCB measured in primary cultured neurons. a, Fluorescence microscopy images and fluorescence response measured in neurons coexpressing R^{ncp}–iGluSnFR (red) and eCB2.0 (green). Similar results were observed for more than 20 neurons. Scale bar, 200 μm. **b**, Fluorescence microscopy images and fluorescence response measured in eCB2.0-expressing neurons preloaded with Calbryte 590 (red). Similar results were observed for more than 20 neurons. Scale bar, 200 μm. **c**, Relative peak change in eCB2.0 fluorescence plotted against the relative peak change in Calbryte 590 (Cal590) fluorescence measured in response to the indicated number of electrical pulses, normalized to the response evoked by 200 pulses; $n = 4$ cultures each, mean ± s.e.m. Also shown is the response to 20 electrical pulses with no extracellular (extra) Ca^{2+}. **d**, Diagram depicting the pathway for eCB synthesis. DAG, diacylglycerol; DAGL, diacylglycerol lipase. **e**, Representative traces (left) and expanded traces (right) showing the change in eCB2.0 fluorescence in responses to 20 electrical pulses applied before (1) and after (2) DO34 application; WIN55212-2 was applied at the end of the experiment. **f**, Summary of the peak change in eCB2.0 fluorescence in response to 20 pulses applied at baseline (Ctrl), 26 min after DO34 application (DO) and after WIN55212-2 application (WIN); $n = 3$ cultures each, mean ± s.e.m. A paired two-tailed Student's *t*-test was performed ($P = 0.0004$). **g**, Diagram depicting degradation pathways for 2-AG and AEA. AA, arachidonic acid; MAGL, monoacylglycerol lipase; FAAH, fatty acid amide hydrolase. **h**, Representative traces (left) and expanded traces (right) showing the change in eCB2.0 fluorescence in response to 20 electrical pulses applied before (1) and after (2) JZL184 or URB597 application; AM251 was applied at the end of the experiment. **i**, Summary of the decay time constant (τ_{decay}) measured at baseline (Ctrl) and 68 min after application of either JZL184 (JZL) or URB597 (URB); $n = 3$ and 4 cultures each, mean ± s.e.m. Paired two-tailed Student's *t*-tests were performed ($P = 0.0462$ (left) and $P = 0.0354$ (right)). **j**, Pseudocolor images showing spontaneous changes in eCB2.0 fluorescence transients, single-pulse-evoked fluorescence change and the change in fluorescence induced by 10 μM WIN55212-2 (note the difference in scale). Scale bar, 100 μm. **k**, Time-lapse pseudocolor images taken from the area shown by the bottom dashed rectangle in **j**. Scale bar, 10 μm. Stim, stimulation. **l**, Traces from the experiment shown in **k**, showing the change in fluorescence measured spontaneously, induced by a single pulse or in the presence of AM251. Normalized traces with the corresponding rise time constants are shown at the right. Spon, spontaneous. **m**, Spatial profile of the transient change in fluorescence shown in **k**. Summary data are shown at the right with the mean labeled; $n = 42$ transients from three cultures, mean ± s.e.m. FWHM, full-width at half-maximum. **n**, Cumulative transient change in eCB2.0 fluorescence measured during a 19-min recording in the absence (left) or presence (right) of AM251. Pseudocolor images were calculated as the average temporal projection subtracted from the maximum temporal projection. Scale bar, 100 μm. **o**, Summary of the frequency of transient changes in eCB2.0 fluorescence measured before (Ctrl) and after AM251 application; $n = 5$ and $n = 3$ with 10 min of recording per session. Boxes show the first and third quartiles as well as the median (line), and whiskers extend to the most extreme data point that is no more than 1.5× the interquartile range from the box. A two-tailed Student's *t*-test was performed ($P = 5.79 \times 10^{-6}$). $^{***}P < 0.001$, $^{*}P < 0.05$.

effect on CB1R-mediated signals (Extended Data Fig. 3g,h). Second, we used a bioluminescence resonance energy transfer (BRET) sensor to detect $G_{\beta\gamma}$ activation. Treating cells expressing CB1R with 2-AG induced a robust increase in BRET, consistent with G protein activation; by contrast, 2-AG had no effect on BRET in mock-transfected control cells or in cells expressing either eCB2.0 or eCBmut (Extended Data Fig. 3i). In addition, we also measured β-arrestin recruitment using the Tango GPCR assay[45] and found that AEA induced a robust, concentration-dependent response in cells expressing CB1R but had no effect in control cells or cells expressing either eCB2.0 or eCBmut (Extended Data Fig. 3j). Lastly, we tested eCB2.0 in HEK293T cells with or without coexpression of CB1R and found that CB1R did not change the dose-dependent response of eCB2.0 to 2-AG (Extended Data Fig. 3k). In sum, these data indicate that the eCB2.0 sensor binds eCBs but does not couple to downstream effector proteins or affect

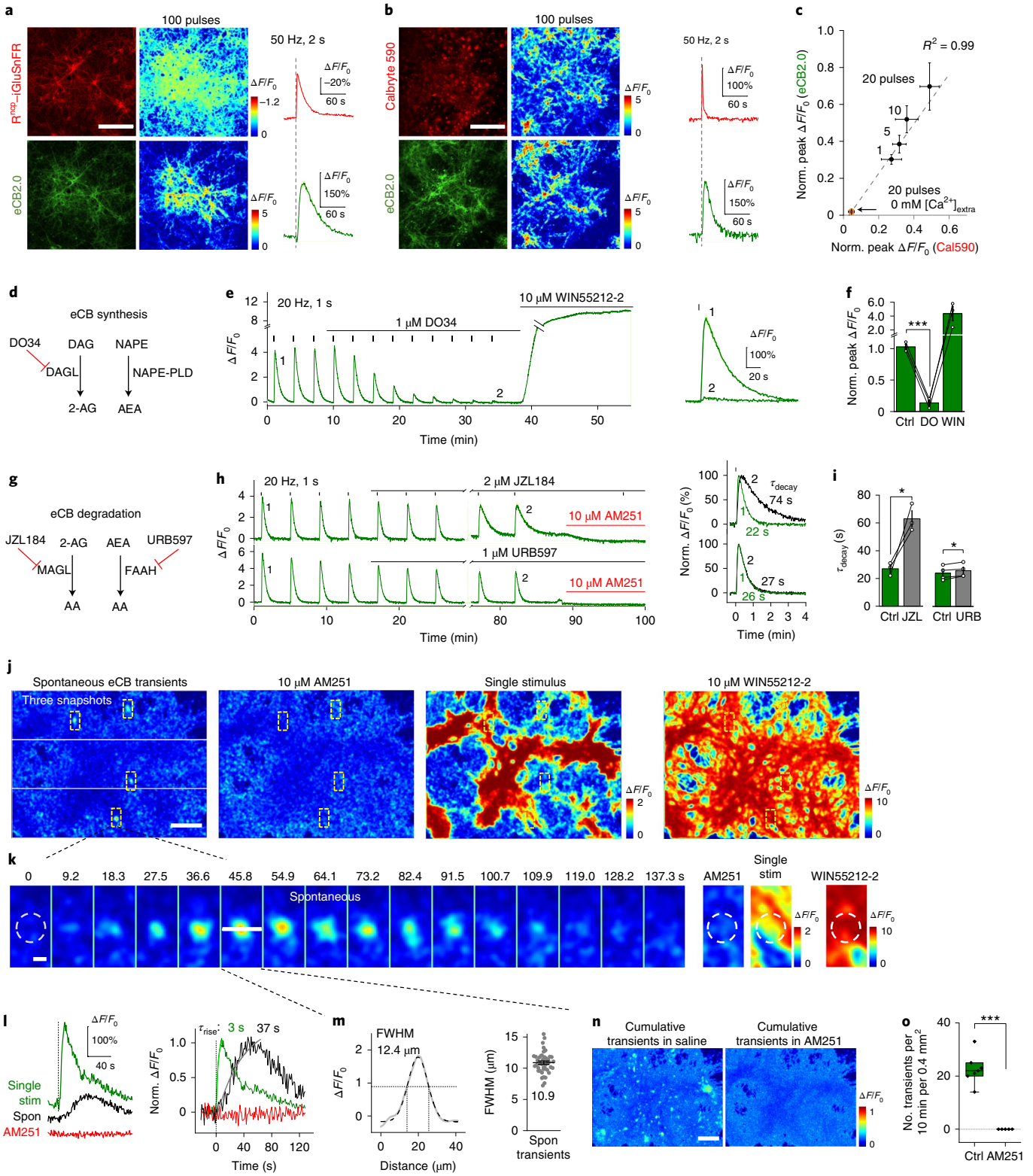

CB1R-mediated signals and therefore likely does not affect cellular physiology; conversely, eCB2.0 is not significantly buffered by CB1R expression either.

We next examined the expression pattern of the eCB sensor in neurons by sparsely expressing eCB2.0 in cultured rat cortical neurons using calcium phosphate transfection. We found that eCB2.0 trafficked to the entire neuronal cell membrane, including axons and dendrites, as shown by colocalization with the axonal presynaptic marker synaptophysin–mScarlet and the postsynaptic marker PSD95–mScarlet (Fig. 2a). To measure the response of eCB2.0 in neurons, we infected cultured rat cortical neurons using an adeno-associated virus (AAV) expressing either eCB2.0 or eCBmut under the control of the human *SYN1* (synapsin) promoter to drive expression in all neurons (Fig. 2b). We found that both 2-AG and AEA elicited concentration-dependent fluorescence responses in neurons expressing eCB2.0, with maximum fluorescence increases of 950% and 500% and EC_{50} values of 9.0 µM and 0.8 µM, respectively; by contrast, neither 2-AG nor AEA elicited a response in neurons expressing eCBmut, even at 100 µM (Fig. 2b,c). We also found that eCB2.0 responses in neurites were higher than those in somata (Fig. 2d). Finally, bath application of the CB1R agonist WIN55212-2, which can activate eCB2.0 in HEK293T cells, to eCB2.0-expressing neurons induced a fluorescence increase that was stable for up to 2 h and was blocked completely by AM251 (Fig. 2e), suggesting that the sensor does not undergo arrestin-mediated internalization or desensitization and can be used for long-term monitoring of eCB activity.

Imaging eCB in primary cultured neurons. Cultured neurons are commonly used for studying eCB-mediated synaptic modulation[26]. We therefore investigated whether our eCB2.0 sensor could be used to detect the release of endogenous eCB in cultured rat cortical neurons expressing eCB2.0 together with a red glutamate sensor R^{ncp}–iGluSnFR[46]. Applying electrical field stimuli (100 pulses at 50 Hz) elicited robust eCB and glutamate signals (Fig. 3a), demonstrating that eCB2.0 can reliably report endogenous eCB release and is compatible with red fluorescent indicators. Importantly, expression of eCB2.0 did not affect electrically evoked R^{ncp}–iGluSnFR signals in neurons compared with those in control neurons, indicating that eCB2.0 has a minimal effect on neuronal glutamate release (Extended Data Fig. 4). We then expressed eCB2.0 in neurons loaded with a red fluorescent Ca^{2+} dye, Calbryte 590, to simultaneously measure eCB release and changes in intracellular Ca^{2+} levels. Field stimuli (100 pulses at 50 Hz) elicited robust responses with respect to both intracellular Ca^{2+} elevation and eCB release (Fig. 3b). Moreover, rise and decay kinetics of the Ca^{2+} signal were faster than those of the eCB signal, consistent with the notion that eCB release requires neuronal activity[47]. We also found a strong correlation between the peak Ca^{2+} signal and the peak eCB signal when applying increasing numbers of stimuli ($R^2 = 0.99$, Fig. 3c); importantly, in the absence of extracellular Ca^{2+}, even 20 pulses were unable to elicit either a Ca^{2+} signal or an eCB2.0 response (Fig. 3c), confirming the requirement of Ca^{2+} activity for eCB release.

Next, we asked which specific eCB (2-AG and/or AEA) is released from cultured rat cortical neurons. The eCB 2-AG is mainly produced in neurons from diacylglycerol by diacylglycerol lipase, while AEA is mainly produced from *N*-arachidonoyl phosphatidylethanolamine (NAPE) by the enzyme NAPE-hydrolyzing phospholipase D (NAPE-PLD) (Fig. 3d). We found that the selective diacylglycerol lipase inhibitor DO34 (ref. [48]) eliminated the stimulus-evoked eCB2.0 signal within 30 min; as a positive control, subsequent application of the CB1R agonist WIN55212-2 restored eCB2.0 fluorescence, indicating that the sensor was still present in the cell membrane (Fig. 3e,f). We also examined the effect of blocking the degradation of 2-AG and AEA by the enzymes monoacylglycerol lipase and fatty acid amide hydrolase using the inhibitors JZL184 (ref. [49]) and URB597 (ref. [50]), respectively (Fig. 3g). We found that blocking monoacylglycerol lipase significantly increased the decay time constant, while blocking fatty acid amide hydrolase had only a slight, albeit significant, effect on the decay time constant (Fig. 3h,i). In sum, these data indicate that 2-AG is the principal eCB released from cultured rat cortical neurons in response to electrical stimuli. Lastly, to estimate the concentration of 2-AG released from neurons, we recorded fluorescence responses of eCB2.0 evoked by one to 100 electrical pulses at 20 Hz and then calibrated sensor responses versus exogenous 2-AG applied at different concentrations. Using the calibration curve, we estimated that 0.5–7.7 µM 2-AG was released from cultured cortical neurons after electrical stimulation (Extended Data Fig. 5).

In addition to stimulus-evoked eCB signals, we also observed local, transient eCB2.0 signals in neurons that occurred spontaneously in the absence of external stimulation (Fig. 3j). Peak amplitude and rise kinetics of these transient eCB2.0 signals were smaller and slower than those of the signal measured in response to a single electrical stimulus in the same region of interest (ROI) (Fig. 3k,l), suggesting that evoked and spontaneous eCB release have distinct patterns. The average diameter of spontaneous transient signals was ~11 µm based on our analysis of full-width at half-maximum (Fig. 3m), consistent with previous suggestions that eCB acts locally[51,52], although the value might be a lower estimate limited by the sensor's sensitivity. Finally, the spontaneous transient was no longer observed after application of the CB1R inverse agonist AM251 or the CB1R neutral antagonist NESS0327, while the action potential blocker tetrodotoxin did not block spontaneous signals (Fig. 3l,n,o and Extended Data Fig. 6).

Fig. 4 | Using the $GRAB_{eCB}$ sensor to detect eCB release in acute brain slices. a, Schematic diagram depicting the strategy for viral injection into the DLS, followed by preparation of acute brain slices used for electrical stimulation and photometry recording. The dashed box corresponds to the image shown in **b**. **b**, Fluorescence image of a coronal slice prepared from a mouse following injection of AAV-syn-eCB2.0 into the DLS, with a diagram showing the electrode position and photometry recording. Similar results were observed for more than six slices. Scale bar, 1 mm. Obj, objective. **c**, Representative traces showing the change in eCB2.0 fluorescence evoked by two, five or ten electrical pulses applied at the indicated frequencies (freq). **d**, Peak change in eCB2.0 fluorescence (left), rise $t_{1/2}$ (middle) and decay time constant (right) plotted against stimulation frequency for two, five and ten pulses; $n = 6$ slices, mean ± s.e.m. **e**, Representative traces (left) and summary of the peak change in eCB2.0 fluorescence (right) evoked by electrical pulses at the indicated frequency in slices expressing eCB2.0 in the absence or presence of AM251 and in slices expressing eCBmut; $n = 4$ slices for eCB2.0 and AM251 groups, $n = 3$ for the eCBmut group, mean ± s.e.m. **f**, Schematic diagram depicting the strategy for viral expression in the hippocampal CA1 of CB1R-P2A-FlpO mice and the expression of eCB2.0 in CB1R-positive neurons. Or, oriens; py, pyramidal; rad, radiatum. **g**, Fluorescence images of eCB2.0 expressed in the CA1 region in conditions with saline (left) and a 75 mM K^+ solution (middle). Right: pseudocolor images showing the change in eCB2.0 fluorescence after perfusion with the 75 mM K^+ solution. Images at the bottom are taken from the area shown by the dashed yellow box at the top. Similar results were observed for more than five slices. Scale bars, 20 µm (top) and 5 µm (bottom). **h**, Representative images and three-dimensional illustration showing a bouton during conditions of baseline, spontaneous eCB release and eCB release induced by 75 mM K^+. Arrows indicate time points of the three representative images during the recording. Scale bar, 2 µm; a.u., arbitrary units. **i**, Spatial profile of the transient change in fluorescence from a single bouton shown in **h**. Summary data are shown at the right; $n = 6$ and 21 boutons, mean ± s.e.m. **j**, Left: temporal profile of the transient change in fluorescence from a single bouton shown in **h**. Right: summary data of $t_{1/2}$ and peak $\Delta F/F_0$; $n = 6$ and 21 boutons, mean ± s.e.m.

Imaging eCB in acute mouse brain slices. Next, we examined whether our eCB sensor can be used to detect endogenous eCB release in a more physiologically relevant system, namely acute mouse brain slices. We first injected AAVs expressing either eCB2.0 or eCBmut into the dorsolateral striatum (DLS) of adult mice (Fig. 4a), the region where eCB mediates both short-term and long-term depression and regulates motor behavior[53,54]. Four weeks after AAV injection, acute brain slices were prepared, showing expression of eCB sensors in the DLS (Fig. 4b). Fluorescence signals evoked by electrical stimuli in the DLS were recorded by photometry.

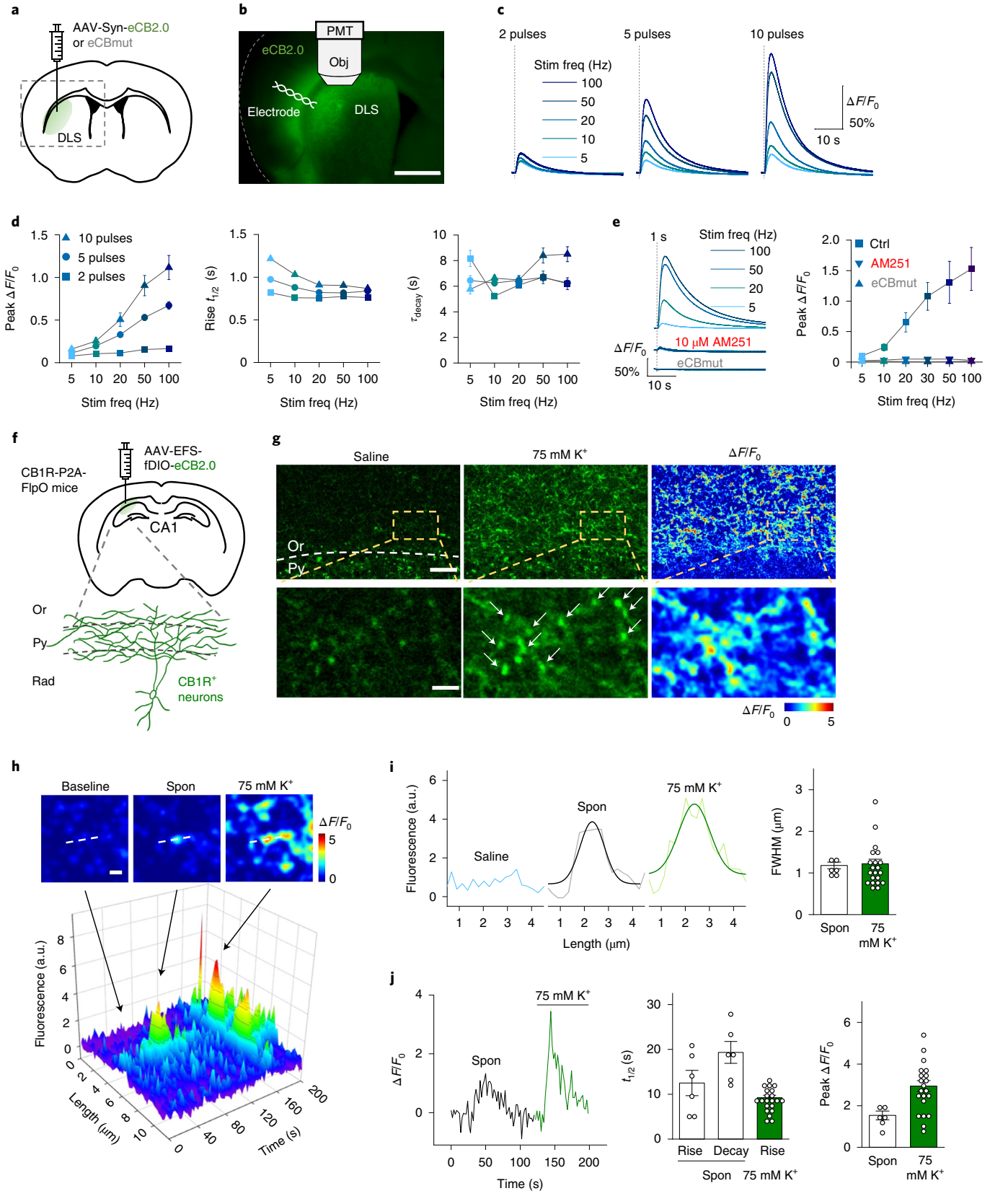

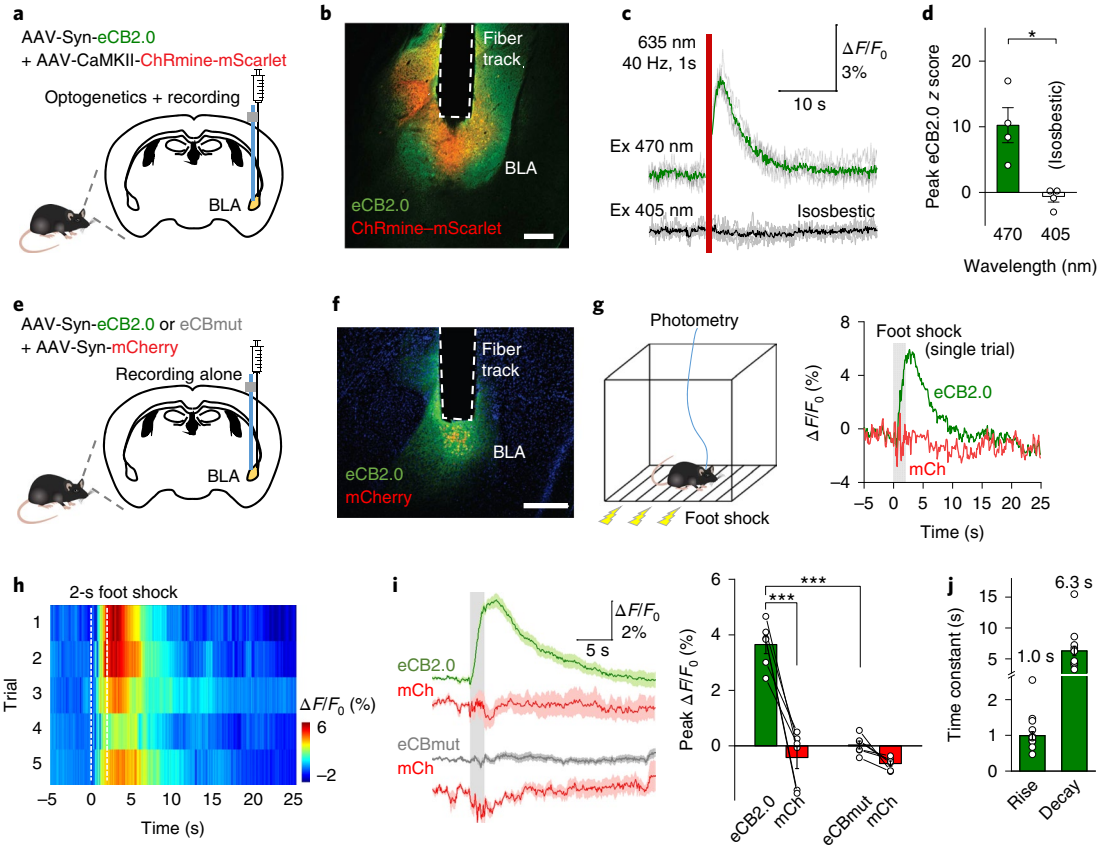

Fig. 5 | Measuring in vivo eCB signals in the mouse BLA in response to foot shock. a, Schematic diagram depicting the strategy for viral expression in the BLA, optogenetic stimulation and fiber photometry recording. **b**, Immunofluorescence image showing eCB2.0 (green) and ChRmine (red) expressed in the BLA and the placement of the recording fiber. Similar results were observed for four mice. Scale bar, 200 µm. **c**, Representative traces of the change in eCB2.0 fluorescence (averaged green trace with five single-trial gray traces) in response to 635-nm laser stimulation in the BLA of one mouse; isosbestic signals (averaged black trace with five single-trial gray traces) were used to monitor potential movement artifacts. **d**, Quantification of peak amplitudes (*z* score) of signals in all mice; $n = 4$ mice, mean ± s.e.m. A paired two-tailed Student's *t*-test was performed ($P = 0.0418$). **e**, Schematic diagram depicting the strategy for viral expression in the BLA. **f**, Immunofluorescence image showing eCB2.0 (green) and mCherry (red) expressed in the BLA and the placement of the recording fiber; nuclei were counterstained with 4,6-diamidino-2-phenylindole (DAPI) (blue). Similar results were observed for six mice. Scale bar, 300 µm. **g**, Schematic diagram depicting fiber photometry recording during foot shock and representative single-trial traces of the change in eCB2.0 and mCherry fluorescence; an electrical foot shock (duration of 2 s) was applied at time 0. **h**, Pseudocolor change in eCB2.0 fluorescence before and after a 2-s foot shock. Shown are five consecutive trials in one mouse, aligned to the time of onset of each foot shock. **i**, Left: average traces of the change in eCB2.0 and mCherry (mCh) (top) and eCBmut and mCherry (bottom) fluorescence; the gray shaded area indicates application of an electrical foot shock. Right: summary of the peak change in fluorescence; $n = 6$ mice each, mean ± s.e.m. Paired two-tailed Student's *t*-tests (between eCB2.0 and mCherry) and two-tailed Student's *t*-tests (between eCB2.0 and eCBmut) were performed ($P = 0.0009$ and 1.35×10^{-6}). **j**, Summary of rise and decay time constants measured for the change in eCB2.0 fluorescence in response to foot shock; $n = 21$ trials for rise measurement and $n = 18$ trials for decay measurement from six animals, mean ± s.e.m. $^{***}P < 0.001$, $^{*}P < 0.05$.

We found that applying electrical stimuli in eCB2.0-expressing slices evoked clear fluorescence signals, and stronger responses were evoked by increasing the number of stimuli and by increasing the stimulation frequency (Fig. 4c,d). The half-rise time and decay time constant ranged from 0.8 to 1.2 s and from 5.2 to 8.5 s (Fig. 4d). Moreover, the signal was specific to eCB release, as pretreating slices with 10 µM AM251 blocked the response and no response was measured in slices expressing the eCBmut mutant sensor (Fig. 4e). Under the five-pulse 100-Hz stimulation condition, the eCB signal was mainly from 2-AG, while AEA likely contributed to a small portion of the signal (Extended Data Fig. 7a–c). In a separate experiment, we performed electrophysiological recording of spontaneous inhibitory postsynaptic currents (sIPSCs) on medium spiny neurons in acute striatal slices and observed eCB-mediated depolarization-induced suppression of inhibition (DSI) (Extended Data Fig. 7d–f). Importantly, DSI was also successfully induced in eCB2.0-expressing striatal slices, suggesting that eCB2.0 expression has minimal influence on endogenous eCB-mediated modulation of synaptic plasticity (Extended Data Fig. 7d–f). We also expressed eCB2.0 in the hippocampal cornu ammonis (CA)1 and BLA regions (Extended Data Fig. 8), where eCB modulates synaptic inputs[21,55,56], and then recorded eCB2.0 signals in acute slices using 2P microscopy. We found that applying an increasing number of electrical stimuli at 20 Hz evoked increasingly larger changes in eCB2.0 fluorescence (Extended Data Fig. 8b,c,g,h) in the CA1 and the BLA; perfusion with 75 mM K^+ induced a larger increase in eCB2.0 fluorescence in the BLA (Extended Data Fig. 8i). In addition, applying 10 µM AEA to hippocampal slices caused a profound increase in eCB2.0 fluorescence that was reversed by 10 µM AM251 (Extended Data Fig. 8d). Finally, AM251 treatment eliminated the signal induced by even 100 field stimuli (Extended Data Fig. 8e).

To further examine the spatial resolution that eCB2.0 imaging can reach, we injected FlpO recombinase-dependent AAV vectors into the hippocampal CA1 of in-house generated CB1R-P2A-FlpO mice to sparsely express eCB2.0 in CB1R-positive neurons. Acute slices were then prepared and imaged using 2P microscopy (Fig. 4f). Perfusing a 75 mM K^+ solution evoked a large fluorescence response from eCB2.0 in individual boutons (Fig. 4g), which are presynaptic terminals. In some cases, spontaneous eCB2.0 signals were recorded from single boutons (Fig. 4h). The diameter (full width at half-maximum) of signals from single boutons was about 1.2 µm (Fig. 4i), consistent with the size of a presynaptic terminus[57]. Kinetics and the peak fluorescent response were also quantified, benefiting from the temporal resolution and sensitivity of eCB2.0 (Fig. 4j). Together, these in vitro data confirm that eCB2.0 can be used to reliably detect the endogenous release of eCBs in acute brain slices with high sensitivity, specificity and spatiotemporal resolution.

eCB measurement in the BLA of freely moving mice. The BLA is a key brain region mediating fear responses and processing aversive memories[58]. Previous studies found that the CB1R is highly expressed in the BLA and the eCB system in the BLA participates in stress expression[59–61]. We therefore tested whether our eCB2.0 sensor can be used to directly measure eCB dynamics in vivo. First, we injected AAV vectors expressing eCB2.0 as well as the red-shifted channelrhodopsin ChRmine[62] into the mouse BLA (Fig. 5a,b). Through the same optic fiber, we delivered red light to stimulate BLA neurons and simultaneously performed photometry recording of eCB2.0 at the same brain region in living mice. Stimulation for 1 s at 40 Hz with 635-nm light triggered a transient green fluorescence increase in eCB2.0 excited by 470-nm light but not by 405-nm (isosbestic) light (Fig. 5c,d). Next, we injected AAV vectors for expression of either eCB2.0 or eCBmut together with mCherry into the mouse BLA and then performed fiber photometry recording while applying an aversive stimulus (electrical foot shock) (Fig. 5e,f). We found that applying a 2-s foot shock induced a time-locked transient increase in eCB2.0 fluorescence in the BLA (Fig. 5g); this response was highly reproducible over five consecutive trials (Fig. 5h). Importantly, the same foot shock had no effect on either mCherry fluorescence or eCBmut fluorescence (Fig. 5i). Average time constants for rise and decay phases of the eCB2.0 signal were 1.0 s and 6.3 s, respectively (Fig. 5j). To confirm that the expression of eCB2.0 has no negative effect on animal behavior, we performed the open-field test, the elevated plus maze test and fear conditioning and found no behavioral differences between mice expressing GPF (as a control) or eCB2.0 in the BLA bilaterally (Extended Data Fig. 9a–f). These data indicate that eCB2.0 can be used to measure eCB dynamics in vivo in freely moving animals without perturbing animal behavior.

Imaging eCB in the mouse CA1 during running and seizures. Our finding that eCB2.0 can be expressed in the mouse hippocampal CA1 region and then measured in acute slices led us to ask whether we can use this sensor to measure in vivo eCB dynamics in the CA1 region during physiologically relevant activities such as running. We therefore injected AAVs expressing eCB2.0 or eCBmut together with a red Ca^{2+} indicator, jRGECO1a[63], into the mouse hippocampal CA1 region and then conducted head-fixed 2P dual-color imaging through an implanted cannula above the hippocampus (Fig. 6a). Coexpression of eCB2.0 and jRGECO1a was clearly observed in neurons in the CA1 4–6 weeks after viral injection (Fig. 6b). We focused on the stratum pyramidale layer, which is composed of pyramidal neuron somata and interneuron axons, including a class that densely express the CB1R. When mice spontaneously ran on a treadmill (Fig. 6c), we found rapid increases in both Ca^{2+} and eCB signals aligned to the start of running and decreases in both signals when they stopped running (Fig. 6d,e). In the control group, which expressed eCBmut and jRGECO1a, Ca^{2+} signals were intact, while eCBmut showed no change in fluorescence (Fig. 6d,e). Both Ca^{2+} and eCB signals had a similar 10–90% rise time and half-time of the decay phase (Fig. 6f). Lastly, no difference was observed in running speed or distance among control, eCB2.0-expressing and eCBmut-expressing mice (Extended Data Fig. 9g), further demonstrating that eCB sensors have no detectable effect on animal behavior.

Epilepsy is a neurological disease characterized by excessive and synchronous neuronal firing. eCBs are proposed to provide negative feedback during epilepsy to attenuate synaptic activity and protect the nervous system, which is exemplified by the observation that all animals with a compromised eCB system exhibit a pro-epileptic phenotype[64]. To explore whether our eCB2.0 sensor can be used to study seizure-related eCB signals in vivo, we used electrical kindling stimulation[65] of the hippocampus contralateral to the sensor-expressing hemisphere to elicit brief self-terminating seizures (measured using local field potential (LFP) recording) (Fig. 6g).

Fig. 6 | Measuring in vivo eCB dynamics in the mouse hippocampus during running and seizure activity. a, Schematic diagram depicting the strategy for viral expression and cannula placement in the mouse hippocampus. **b**, Left: fluorescence microscopy image showing eCB2.0 expression in the hippocampal CA1 region in a coronal brain slice. Scale bars, 200 µm and 50 µm (inset). Right: in vivo 2P image of the pyramidal layer in the hippocampal CA1 region, showing eCB2.0 (green) and jRGECO1a (red) fluorescence. Scale bar, 50 µm. Max, maximum. **c**, Schematic cartoon illustrating the experiment in which a mouse expressing eCB2.0 and jRGECO1a in the hippocampal CA1 is placed on a treadmill and allowed to run spontaneously while fluorescence is measured using 2P microscopy. **d**, Average traces of eCB2.0 or eCBmut and jRGECO1a transients recorded in the soma of individual neurons in the pyramidal layer upon starting and stopping spontaneous running episodes (dashed lines). **e**, Summary of peak responses in **d**; $n = 7$ and 4 mice each for eCB2.0 and eCBmut, respectively, mean ± s.e.m. Two-tailed Student's *t*-tests were performed between jRGECO1a (jR) and jRGECO1a ($P = 0.5979$); one-tailed Student's *t*-tests were performed between eCB2.0 and eCBmut ($P = 0.0284$). **f**, Summary of rise and decay kinetics of jRGECO1a and eCB2.0 signals measured at the start and end of spontaneous running; $n = 7$ mice, mean ± s.e.m. Paired two-tailed Student's *t*-tests were performed ($P = 0.5954$ (left) and 0.0993 (right)). **g**, Schematic diagram depicting electrode placement and 2P imaging in mice expressing eCB2.0 and jRGECO1a in the hippocampal CA1 region; the electrode is used to induce kindling seizure activity and to measure the LFP. **h**, Example LFP trace (top) and mediolateral (ML) projections (line profile) of jRGECO1a (middle) and eCB2.0 (bottom) fluorescence during stimulus-induced nonconvulsive seizures and a subsequent spreading wave. The dotted vertical line at time 0 indicates stimulus onset. **i**, Individual (thin gray lines) and average (thick lines) traces of the change in jRGECO1a and eCB2.0 or eCBmut fluorescence measured during seizure activity. The dashed vertical line at time 0 indicates stimulus onset. The summary of the area under the curve (AUC) is shown at the right; $n = 8$ and 4 for eCB2.0 and eCBmut, respectively, mean ± s.e.m. Two-tailed Student's *t*-tests were performed ($P = 0.2607$ (between jRGECO1a and jRGECO1a) and $P = 0.00098$ (between eCB2.0 and eCBmut)). **j**, Spreading eCB wave measured through the hippocampal CA1 region after seizure activity. ROI representing individual neurons are pseudocolored based on the peak time of their eCB2.0 (2.0) signal relative to the peak time of the average signal, and the arrow shows the direction of the wave. A, anterior; L, lateral; M, medial; P, posterior. **k**, Traces of eCB2.0 fluorescence measured in individual cells sampled systematically along a line fitted to the spreading wave. The dashed line shows the spreading of peak signals. **l**, Velocity and direction of the spreading jRGECO1a and eCB2.0 waves. The length of each arrow indicates velocity in µm s^{-1}. In each panel, each colored arrow indicates an individual session, and the thick black line indicates the average. $n = 7$ sessions in six mice. $^{***}P < 0.001$; $^{*}P < 0.05$; NS, not significant.

We found strong increases in both Ca^{2+} and eCB signals during electrical seizure activity (Fig. 6h). Recent work has shown that seizures are often followed by a spreading Ca^{2+} wave that propagates across the cell layer[65]. Interestingly, we also found a propagating eCB wave that closely followed the Ca^{2+} wave (Fig. 6h, Extended Data Fig. 10 and Supplementary Video 1). By contrast, eCBmut showed no response during or after seizures (Fig. 6i). The velocity and direction of eCB waves were evident when we extracted the eCB2.0 signal from individual neurons in the field of view (Fig. 6j,k). Notably, eCB waves and Ca^{2+} waves varied across experiment sessions and animals (Fig. 6l), but, for each instance, Ca^{2+} and eCB waves were similar, in agreement with the Ca^{2+} and activity dependence of the eCB signal. In sum, our results confirm that the eCB2.0 sensor can be used to measure eCB dynamics in vivo under both physiological and pathological conditions, with high specificity and spatiotemporal resolution.

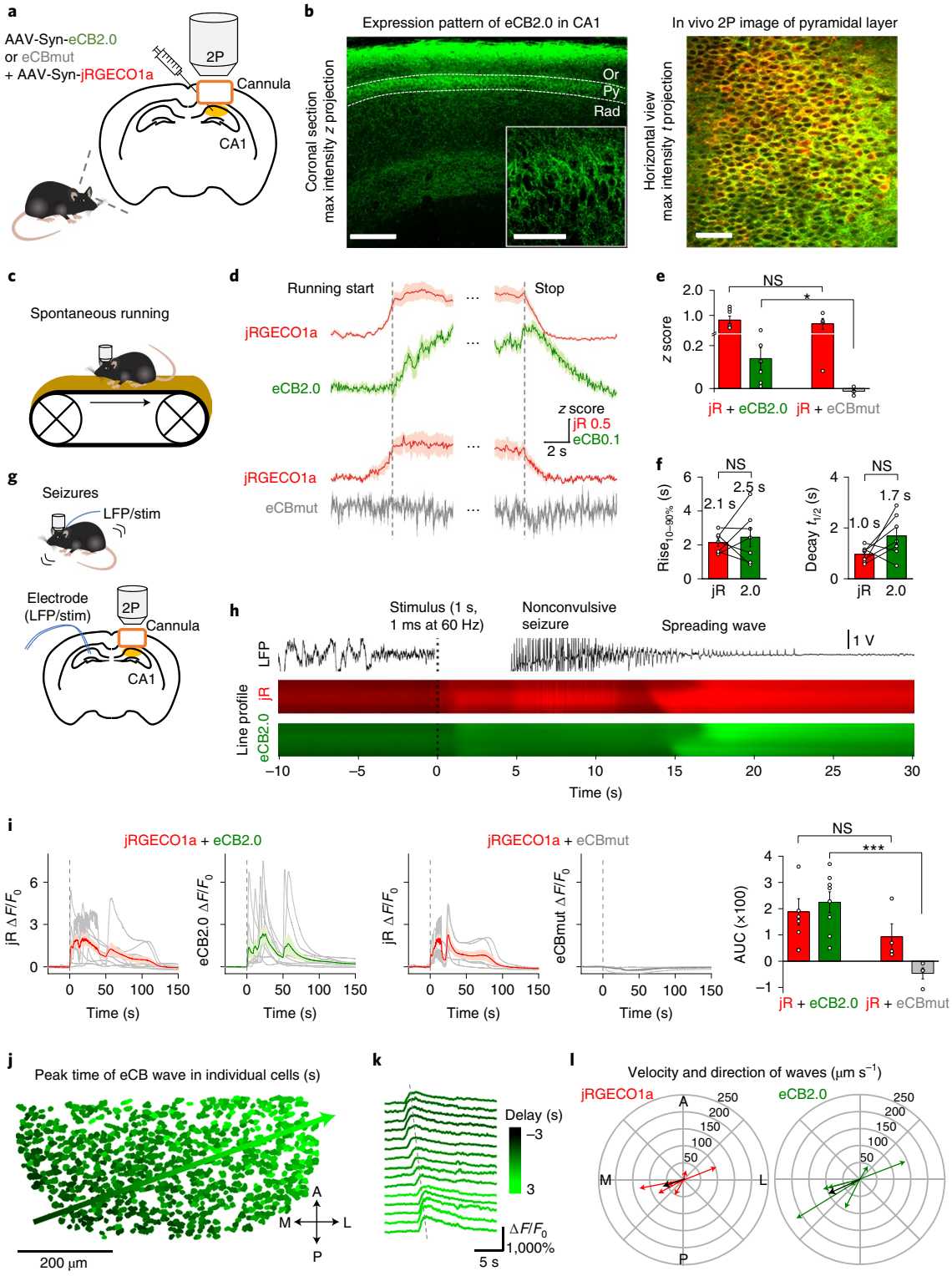

Discussion

Here, we report the development and characterization of a genetically encoded fluorescent sensor for detecting eCBs both in vitro and in vivo. With high sensitivity, selectivity and kinetics, this new eCB sensor can be used to detect endogenous eCB release in cultured neurons, acute brain slices and specific brain structures in vivo such as the amygdala and hippocampus during both physiological and pathological activities.

The dynamic range of eCB2.0 in neurons is higher than that in HEK293T cells, possibly because membrane trafficking of eCB2.0 is better in neurons. Our estimates of τ_{on} and τ_{off} kinetics measured for eCB2.0 in cultured cells at room temperature is likely high, given that a faster time constant was measured in acute slices and in our in vivo experiments; this difference may come from the distinct experimental setup, instrumentation, temperature and eCB source. Nevertheless, given that the temporal resolution of eCB2.0 is on the order of seconds, this tool is a vast improvement compared to microdialysis (with temporal resolution on the order of minutes), although the sensor's kinetics can be improved even further to capture more rapid signals[66]. eCB2.0's apparent affinities for AEA and 2-AG are in the submicromolar and micromolar range, respectively. The relatively lower affinity for 2-AG may prevent the sensor from detecting small amounts of 2-AG. Improved sensors with higher affinities or larger dynamic ranges will be more useful in detecting mild eCB activities. In addition, the eCB2.0 sensor can detect both 2-AG and AEA; given that 2-AG and AEA regulate distinct pathways and are involved in different brain regions and cell types[4], next-generation $GRAB_{eCB}$ sensors should be developed with non-overlapping eCB specificity, as well as non-overlapping color spectra.

Retrograde modulation of synaptic activity by eCBs was previously identified by studying DSI and depolarization-induced suppression of excitation in the hippocampus and cerebellum[21,24,26]. However, because these experiments and subsequent studies used electrophysiological recordings of synaptic transmission combined with either pharmacological interventions or genetic manipulation, they lacked the ability to directly measure eCB release. Recording at the cell body of a neuron does not provide precise spatial information with respect to eCB release. For example, DSI recorded using paired whole-cell recordings in hippocampal slices indicates that depolarization of one neuron can inhibit GABAergic input to neurons within approximately 20 µm, suggestive of the upper limit of diffusion for eCBs from a single neuron[21]; similar results were obtained in cerebellar slices using two separate stimulating electrodes to evoke eCB release from two dendritic regions in a single Purkinje cell[51]. Although these data indicate that eCB signaling is relatively localized and tightly controlled, the detailed spatial profile of eCB signaling is unknown. In addition, eCB signals measured by changes in evoked postsynaptic currents have a sampling interval of approximately 2 s, creating a temporal bottleneck. In this respect, our eCB2.0 sensor can reveal eCB signals with considerably higher spatial and temporal resolution.

In summary, we show that our eCB2.0 sensor can be used in a variety of in vitro and in vivo preparations to monitor eCB dynamics in real time. Given the complexity of the nervous system, future directions for research based on eCB sensor applications may include the identity of cell types that release eCBs, mechanisms and temporal properties of eCB release, characteristics of eCB diffusion, the duration of eCB signals, the nature of cell types and subcellular elements targeted by eCBs and effects on the latter. Answering these fundamental questions will substantially enrich our understanding of the mechanisms and functions of eCB signaling at the synapse and neural circuit levels. Lastly, altered function of the eCB system has been associated with several neurological disorders, including stress or anxiety, movement disorders, substance-use disorders and epilepsy. In this respect, our in vivo results show clear examples of how the eCB2.0 sensor can help to elucidate rapid eCB dynamics during both physiological and pathological processes. Thus, eCB sensors open a new era of eCB research aimed at understanding this system at unprecedented, physiologically relevant spatial and temporal scales.

Online content

Any methods, additional references, Nature Research reporting summaries, source data, extended data, supplementary information, acknowledgements, peer review information; details of author contributions and competing interests; and statements of data and code availability are available at https://doi.org/10.1038/s41587-021-01074-4.

Received: 20 October 2020; Accepted: 27 August 2021;
Published online: 11 November 2021

References

1. Zuardi, A. W. History of cannabis as a medicine: a review. *Braz. J. Psychiatry* **28**, 153–157 (2006).
2. Piomelli, D. The molecular logic of endocannabinoid signalling. *Nat. Rev. Neurosci.* **4**, 873–884 (2003).
3. Wilson, R. I. & Nicoll, R. A. Endocannabinoid signaling in the brain. *Science* **296**, 678–682 (2002).
4. Kano, M., Ohno-Shosaku, T., Hashimotodani, Y., Uchigashima, M. & Watanabe, M. Endocannabinoid-mediated control of synaptic transmission. *Physiol. Rev.* **89**, 309–380 (2009).
5. Hebert-Chatelain, E. et al. A cannabinoid link between mitochondria and memory. *Nature* **539**, 555–559 (2016).
6. Benard, G. et al. Mitochondrial CB1 receptors regulate neuronal energy metabolism. *Nat. Neurosci.* **15**, 558–564 (2012).
7. Jimenez-Blasco, D. et al. Glucose metabolism links astroglial mitochondria to cannabinoid effects. *Nature* **583**, 603–608 (2020).
8. Stella, N. Cannabinoid signaling in glial cells. *Glia* **48**, 267–277 (2004).
9. Navarrete, M., Diez, A. & Araque, A. Astrocytes in endocannabinoid signalling. *Phil. Trans. R Soc. Lond. B* **369**, 20130599 (2014).
10. Chevaleyre, V., Takahashi, K. A. & Castillo, P. E. Endocannabinoid-mediated synaptic plasticity in the CNS. *Annu. Rev. Neurosci.* **29**, 37–76 (2006).
11. Oddi, S., Scipioni, L. & Maccarrone, M. Endocannabinoid system and adult neurogenesis: a focused review. *Curr. Opin. Pharmacol.* **50**, 25–32 (2020).
12. Moreira, F. A. & Lutz, B. The endocannabinoid system: emotion, learning and addiction. *Addict. Biol.* **13**, 196–212 (2008).
13. Guindon, J. & Hohmann, A. G. The endocannabinoid system and pain. *CNS Neurol. Disord. Drug Targets* **8**, 403–421 (2009).
14. Kesner, A. J. & Lovinger, D. M. Cannabinoids, endocannabinoids and sleep. *Front. Mol. Neurosci.* **13**, 125 (2020).
15. Silvestri, C. & Di Marzo, V. The endocannabinoid system in energy homeostasis and the etiopathology of metabolic disorders. *Cell Metab.* **17**, 475–490 (2013).
16. Katona, I. & Freund, T. F. Endocannabinoid signaling as a synaptic circuit breaker in neurological disease. *Nat. Med.* **14**, 923–930 (2008).
17. Fernandez-Espejo, E., Viveros, M. P., Nunez, L., Ellenbroek, B. A. & Rodriguez de Fonseca, F. Role of cannabis and endocannabinoids in the genesis of schizophrenia. *Psychopharmacology* **206**, 531–549 (2009).
18. Fraguas-Sanchez, A. I., Martin-Sabroso, C. & Torres-Suarez, A. I. Insights into the effects of the endocannabinoid system in cancer: a review. *Br. J. Pharmacol.* **175**, 2566–2580 (2018).
19. Patel, S., Hill, M. N., Cheer, J. F., Wotjak, C. T. & Holmes, A. The endocannabinoid system as a target for novel anxiolytic drugs. *Neurosci. Biobehav. Rev.* **76**, 56–66 (2017).
20. Ligresti, A., Petrosino, S. & Di Marzo, V. From endocannabinoid profiling to 'endocannabinoid therapeutics'. *Curr. Opin. Chem. Biol.* **13**, 321–331 (2009).
21. Wilson, R. I. & Nicoll, R. A. Endogenous cannabinoids mediate retrograde signalling at hippocampal synapses. *Nature* **410**, 588–592 (2001).
22. Zoerner, A. A. et al. Quantification of endocannabinoids in biological systems by chromatography and mass spectrometry: a comprehensive review from an analytical and biological perspective. *Biochim. Biophys. Acta* **1811**, 706–723 (2011).
23. Marchioni, C. et al. Recent advances in LC–MS/MS methods to determine endocannabinoids in biological samples: application in neurodegenerative diseases. *Anal. Chim. Acta* **1044**, 12–28 (2018).
24. Kreitzer, A. C. & Regehr, W. G. Retrograde inhibition of presynaptic calcium influx by endogenous cannabinoids at excitatory synapses onto Purkinje cells. *Neuron* **29**, 717–727 (2001).

25. Maejima, T., Hashimoto, K., Yoshida, T., Aiba, A. & Kano, M. Presynaptic inhibition caused by retrograde signal from metabotropic glutamate to cannabinoid receptors. *Neuron* **31**, 463–475 (2001).
26. Ohno-Shosaku, T., Maejima, T. & Kano, M. Endogenous cannabinoids mediate retrograde signals from depolarized postsynaptic neurons to presynaptic terminals. *Neuron* **29**, 729–738 (2001).
27. Wiskerke, J. et al. Characterization of the effects of reuptake and hydrolysis inhibition on interstitial endocannabinoid levels in the brain: an in vivo microdialysis study. *ACS Chem. Neurosci.* **3**, 407–417 (2012).
28. Walker, J. M., Huang, S. M., Strangman, N. M., Tsou, K. & Sanudo-Pena, M. C. Pain modulation by release of the endogenous cannabinoid anandamide. *Proc. Natl Acad. Sci. USA* **96**, 12198–12203 (1999).
29. Sun, F. et al. A genetically encoded fluorescent sensor enables rapid and specific detection of dopamine in flies, fish, and mice. *Cell* **174**, 481–496 (2018).
30. Patriarchi, T. et al. Ultrafast neuronal imaging of dopamine dynamics with designed genetically encoded sensors. *Science* **360**, eaat4422 (2018).
31. Jing, M. et al. A genetically encoded fluorescent acetylcholine indicator for in vitro and in vivo studies. *Nat. Biotechnol.* **36**, 726–737 (2018).
32. Feng, J. et al. A genetically encoded fluorescent sensor for rapid and specific in vivo detection of norepinephrine. *Neuron* **102**, 745–761 (2019).
33. Peng, W. et al. Regulation of sleep homeostasis mediator adenosine by basal forebrain glutamatergic neurons. *Science* **369**, eabb05566 (2020).
34. Patriarchi, T. et al. An expanded palette of dopamine sensors for multiplex imaging in vivo. *Nat. Methods* **17**, 1147–1155 (2020).
35. Jing, M. et al. An optimized acetylcholine sensor for monitoring in vivo cholinergic activity. *Nat. Methods* **17**, 1139–1146 (2020).
36. Sun, F. et al. Next-generation GRAB sensors for monitoring dopaminergic activity in vivo. *Nat. Methods* **17**, 1156–1166 (2020).
37. Wan, J. et al. A genetically encoded sensor for measuring serotonin dynamics. *Nat. Neurosci.* **24**, 746–752 (2021).
38. Howlett, A. C. et al. International Union of Pharmacology. XXVII. Classification of cannabinoid receptors. *Pharmacol. Rev.* **54**, 161–202 (2002).
39. Hua, T. et al. Crystal structures of agonist-bound human cannabinoid receptor CB1. *Nature* **547**, 468–471 (2017).
40. Hua, T. et al. Crystal structure of the human cannabinoid receptor CB1. *Cell* **167**, 750–762 (2016).
41. Krishna Kumar, K. et al. Structure of a signaling cannabinoid receptor 1–G protein complex. *Cell* **176**, 448–458 (2019).
42. Li, X. et al. Crystal structure of the human cannabinoid receptor CB2. *Cell* **176**, 459–467 (2019).
43. Shao, Z. et al. Structure of an allosteric modulator bound to the CB1 cannabinoid receptor. *Nat. Chem. Biol.* **15**, 1199–1205 (2019).
44. Shao, Z. et al. High-resolution crystal structure of the human CB1 cannabinoid receptor. *Nature* **540**, 602–606 (2016).
45. Kroeze, W. K. et al. PRESTO-Tango as an open-source resource for interrogation of the druggable human GPCRome. *Nat. Struct. Mol. Biol.* **22**, 362–369 (2015).
46. Wu, J. et al. Genetically encoded glutamate indicators with altered color and topology. *ACS Chem. Biol.* **13**, 1832–1837 (2018).
47. Alger, B. E. Retrograde signaling in the regulation of synaptic transmission: focus on endocannabinoids. *Prog. Neurobiol.* **68**, 247–286 (2002).
48. Ogasawara, D. et al. Rapid and profound rewiring of brain lipid signaling networks by acute diacylglycerol lipase inhibition. *Proc. Natl Acad. Sci. USA* **113**, 26–33 (2016).
49. Long, J. Z. et al. Selective blockade of 2-arachidonoylglycerol hydrolysis produces cannabinoid behavioral effects. *Nat. Chem. Biol.* **5**, 37–44 (2009).
50. Mor, M. et al. Cyclohexylcarbamic acid 3′- or 4′-substituted biphenyl-3-yl esters as fatty acid amide hydrolase inhibitors: synthesis, quantitative structure–activity relationships, and molecular modeling studies. *J. Med. Chem.* **47**, 4998–5008 (2004).
51. Brenowitz, S. D. & Regehr, W. G. Associative short-term synaptic plasticity mediated by endocannabinoids. *Neuron* **45**, 419–431 (2005).
52. Soler-Llavina, G. J. & Sabatini, B. L. Synapse-specific plasticity and compartmentalized signaling in cerebellar stellate cells. *Nat. Neurosci.* **9**, 798–806 (2006).
53. Gerdeman, G. L., Ronesi, J. & Lovinger, D. M. Postsynaptic endocannabinoid release is critical to long-term depression in the striatum. *Nat. Neurosci.* **5**, 446–451 (2002).
54. Kreitzer, A. C. & Malenka, R. C. Endocannabinoid-mediated rescue of striatal LTD and motor deficits in Parkinson's disease models. *Nature* **445**, 643–647 (2007).
55. Peterfi, Z. et al. Endocannabinoid-mediated long-term depression of afferent excitatory synapses in hippocampal pyramidal cells and GABAergic interneurons. *J. Neurosci.* **32**, 14448–14463 (2012).
56. Ohno-Shosaku, T. et al. Presynaptic cannabinoid sensitivity is a major determinant of depolarization-induced retrograde suppression at hippocampal synapses. *J. Neurosci.* **22**, 3864–3872 (2002).
57. Siksou, L. et al. Three-dimensional architecture of presynaptic terminal cytomatrix. *J. Neurosci.* **27**, 6868–6877 (2007).
58. Li, B. Central amygdala cells for learning and expressing aversive emotional memories. *Curr. Opin. Behav. Sci.* **26**, 40–45 (2019).
59. Katona, I. et al. Distribution of CB1 cannabinoid receptors in the amygdala and their role in the control of GABAergic transmission. *J. Neurosci.* **21**, 9506–9518 (2001).
60. Morena, M., Patel, S., Bains, J. S. & Hill, M. N. Neurobiological interactions between stress and the endocannabinoid system. *Neuropsychopharmacology* **41**, 80–102 (2016).
61. Gunduz-Cinar, O., Hill, M. N., McEwen, B. S. & Holmes, A. Amygdala FAAH and anandamide: mediating protection and recovery from stress. *Trends Pharmacol. Sci.* **34**, 637–644 (2013).
62. Marshel, J. H. et al. Cortical layer-specific critical dynamics triggering perception. *Science* **365**, eaaw5202 (2019).
63. Dana, H. et al. Sensitive red protein calcium indicators for imaging neural activity. *eLife* **5**, e12727 (2016).
64. Soltesz, I. et al. Weeding out bad waves: towards selective cannabinoid circuit control in epilepsy. *Nat. Rev. Neurosci.* **16**, 264–277 (2015).
65. Farrell, J. S. et al. In vivo assessment of mechanisms underlying the neurovascular basis of postictal amnesia. *Sci. Rep.* **10**, 14992 (2020).
66. Heinbockel, T. et al. Endocannabinoid signaling dynamics probed with optical tools. *J. Neurosci.* **25**, 9449–9459 (2005).

Methods

Molecular biology. DNA fragments were amplified by PCR using primers (Tsingke Biological Technology) with 25–30-bp overlaps. Plasmids were constructed using restriction enzyme cloning or Gibson assembly, and all plasmid sequences were verified using Sanger sequencing. To characterize eCB2.0 and eCBmut in HEK293T cells, the corresponding DNA constructs were cloned into the pDisplay vector with an upstream IgK leader sequence. An IRES-mCherry-CAAX cassette was inserted downstream of the sensor gene for labeling the cell membrane and calibrating the sensor's fluorescence. To characterize eCB2.0 in neurons, the eCB2.0 gene was cloned into a pAAV vector under control of a human synapsin (*SYN1*) promoter (pAAV-*hSyn*), and sequences encoding PSD95–mScarlet and synaptophysin–mScarlet were cloned into the pDest vector under the control of the *CMV* promoter. For the $G_{\beta\gamma}$ sensor assay, human *CB1R* was cloned into the pCI vector (Promega), and sequences encoding eCB2.0 and eCBmut were cloned into the peGFP-C1 vector (Takara), replacing the eGFP open reading frame. For the Tango assay, genes for the human CB1R, eCB2.0 and eCBmut were cloned into the pTango vector. In addition, viral vectors pAAV-hsyn-eCBmut and pAAV-hsyn-R^{ncp}-iGluSnFR were generated and used in this study.

AAV expression. AAV2/9-hSyn-eCB2.0 (9.5×10^{13} viral genomes (vg) per ml), AAV2/9-hSyn-eCBmut (8.0×10^{13} vg ml^{-1}), AAV2/9-EFS-fDIO-eCB2.0 (8.3×10^{13} vg ml^{-1}), AAV2/9-hSyn-R^{ncp}-iGluSniFR (6.2×10^{13} vg ml^{-1}, all packaged at Vigene Biosciences), AAV9-CaMKII-ChRmine-mScarlet (K. Deisseroth's laboratory at Stanford University), AAV8-hSyn-mCherry (114472, Addgene), AAV9-CAG-GFP (University of North Carolina Vector Core Facility) and AAV1-Syn-NES-jRGECO1a-WPRE-SV40 (Penn Vector Core) were used to infect cultured neurons or were injected in vivo into specific brain regions.

Cell culture. HEK293T cells were cultured at 37 °C in air containing 5% CO_2 in DMEM (Biological Industries) supplemented with 10% (vol/vol) FBS (Gibco) and penicillin (100 U ml^{-1})–streptomycin (0.1 mg ml^{-1}) (Biological Industries). For experiments, HEK293T cells were plated on 96-well plates or 12-mm glass coverslips in 24-well plates. At 60–70% confluency, cells were transfected by using polyethylenimine with 300 ng DNA per well (for 96-well plates) or 1 μg DNA per well (for 24-well plates) at a DNA:polyethylenimine ratio of 1:3; 4–6 h after transfection, the culture medium was replaced with fresh medium. Imaging was performed 24–36 h after transfection. Rat cortical neurons were prepared from postnatal day 0 (P0) Sprague Dawley rats. In brief, the cerebral cortex was dissected, and cortical neurons were dissociated by digestion in 0.25% trypsin–EDTA (Biological Industries) and then plated on poly-D-lysine-coated (Sigma-Aldrich) 12-mm glass coverslips in 24-well plates. Neurons were cultured at 37 °C with 5% CO_2 in Neurobasal Medium (Gibco) supplemented with 2% B-27 Supplement (Gibco), 1% GlutaMAX (Gibco) and penicillin (100 U ml^{-1})–streptomycin (0.1 mg ml^{-1}) (Biological Industries). For the transfection experiment in Fig. 2a, cultured neurons were transfected at 7–9 d in vitro (DIV7–DIV9) using the calcium phosphate transfection method and imaged 48 h after transfection. For viral infection, cultured neurons were infected with AAVs expressing eCB2.0, eCBmut and/or R^{ncp}–iGluSnFR at DIV3–DIV5 and imaged at DIV12–DIV20. When indicated, neurons were loaded with Calbryte 590 (AAT Bioquest) 1 h before imaging.

Animals. All experimental protocols were approved by the respective laboratory animal care and use committees of Peking University, the National Institute on Alcohol Abuse and Alcoholism, the Cold Spring Harbor Laboratory and Stanford University, and all studies were performed in accordance with guidelines established by the US National Institutes of Health. P0 Sprague Dawley rats (Beijing Vital River Laboratory) of both sexes and P42–P150 C57BL/6J mice (Beijing Vital River Laboratory and Jackson Laboratory) of both sexes were used in this study. The CB1R-P2A-FlpO mouse line was generated by inserting the sequence for P2A-FlpO before the *Cnr1* stop codon using the CRISPR–Cas9 method and was used in this study. Mice were housed at 18–23 °C with 40–60% humidity under a normal 12-h light–dark cycle with food and water available ad libitum.

Confocal imaging of cultured cells. Before imaging, the culture medium was replaced with Tyrode's solution consisting of (in mM): 150 NaCl, 4 KCl, 2 $MgCl_2$, 2 $CaCl_2$, 10 HEPES and 10 glucose (pH 7.4). A solution of 0 mM $[Ca^{2+}]_{ex}$ was modified from Tyrode's solution with 0 mM $CaCl_2$ and additional 2 mM EGTA. HEK293T cells in 96-well plates were imaged using an Opera Phenix high-content screening system (PerkinElmer) equipped with a ×20, 0.4-numerical aperture (NA) objective, a ×40, 0.6-NA objective, a ×40, 1.15-NA water-immersion objective, a 488-nm laser and a 561-nm laser. Green and red fluorescence was collected using 525/50-nm and 600/30-nm emission filters, respectively. Cells in 12-mm coverslips were imaged using a Ti-E A1 confocal microscope (Nikon) equipped with a ×10, 0.45-NA objective, a ×20, 0.75-NA objective, a ×40, 1.35-NA oil-immersion objective, a 488-nm laser and a 561-nm laser. Green and red fluorescence was collected using 525/50-nm and 595/50-nm emission filters, respectively. The following compounds were applied by replacing Tyrode's solution (for imaging in 96-well plates) or by either bath application or using a custom-made perfusion system (for imaging cells on 12-mm coverslips): 2-AG (Tocris), AEA (Cayman), AM251 (Tocris), LPA (Tocris), S1P (Tocris), ACh (Solarbio), dopamine (Sigma-Aldrich), GABA (Tocris), Glu (Sigma-Aldrich), Gly (Sigma-Aldrich), NE (Tocris), 5-HT (Tocris), His (Tocris), Epi (Sigma-Aldrich), Ado (Tocris), Tyr (Sigma-Aldrich), WIN55212-2 (Cayman), CP55940 (Cayman), Δ-9-THC (the Third Research Institute of the Ministry of Public Security), NESS0327 (Cayman), tetrodotoxin (Must Biotech), DO34 (MedChemExpress), JZL184 (Cayman) and URB597 (Cayman). Micropressure application of drugs was controlled with the Pneumatic PicoPump PV800 (World Precision Instruments). Cultured neurons were field stimulated using parallel platinum electrodes positioned 1 cm apart; electrodes were controlled with a Grass S88 stimulator (Grass Instruments), and 1-ms pulses were applied at 80 V. All imaging experiments were performed at room temperature (22–24 °C).

Fluorescent spectrum and photostability measurement. Plasmids for expression of eCB2.0 or EGFP-CAAX were transfected into HEK293T cells in six-well plates (for 1P spectrum measurement) or on 12-mm coverslips (for 2P spectrum and photostability measurements). For 1P spectrum measurement, approximately 24–36 h after transfection, cells were digested with trypsin, washed with PBS, resuspended in Tyrode's solution (or Tyrode's solution containing 100 μM 2-AG) and placed into 384-well plates, in which each well contained cells from one-quarter of cells from a six-well plate well. Control cells transfected with an empty vector were used for background subtraction. Using the Safire 2 plate reader (Tecan), excitation spectra were measured from 350 to 520 nm with a step size of 5 nm and a bandwidth of 20 nm; the emission was set to 560 nm with a 20-nm bandwidth. Emission spectra were measured from 500 to 650 nm with a step size of 5 nm and a bandwidth of 20 nm; excitation was set to 455 nm with a bandwidth of 20 nm. For 2P spectrum measurement, cells in Tyrode's solution or Tyrode's solution containing 100 μM 2-AG were imaged using an Ultima Investigator 2P microscope (Bruker) equipped with a ×20, 1.00-NA objective (Olympus) and an InSight X3 tunable laser (Spectra-Physics). Images were captured when cells were excited from 700 to 1,050 nm with a step size of 10 nm. The fluorescence of untransfected cells was subtracted as background. Laser power was normalized according to the output power of the tunable 2P laser with different wavelengths. Photostability was measured under 1P illumination (confocal laser scanning) using a 488-nm laser with laser power of ~100 μW and under 2P illumination using a 920-nm laser with laser power of ~100 mW.

$G_{q\text{-}i}$ calcium imaging assay. Plasmids for expression of eCB2.0 or CB1R–EGFP were cotransfected into HEK293T cells with a single construct for the expression of jRGECO1a-P2A-$G_{q\text{-}i1}$. Approximately 24–36 h after transfection, cells in 12-mm coverslips were imaged using a Ti-E A1 confocal microscope (Nikon) as described above. Next, 2-AG at the indicated concentrations was applied by bath application and washed using a custom-made perfusion system.

Bioluminescence resonance energy transfer $G_{\beta\gamma}$ sensor assay. The BRET $G_{\beta\gamma}$ sensor was developed based upon similar systems[67,68]. Plasmids for expression of eCB2.0, eCBmut or CB1R were cotransfected into HEK293T cells together with a single construct for the expression of human GNAOa, human GNB1 (fused to amino acids 156–239 of Venus), human GNG2 (fused to amino acids 2–155 of Venus) and NanoLuc fused to the amino-terminal 112 amino acids of human phosducin circularly permutated at amino acids 54 and 55 (Promega). The NanoLuc–phosducin fusion portion also contains a kRAS membrane-targeting sequence at the carboxy-terminal end. Templates for assembly were derived from human whole-brain cDNA (Takara) for all cDNA, except for those for hGNB1 and hGNG2 Venus fusions, which were a generous gift from N. Lambert (Augusta University). Approximately 24 h after transfection, cells were collected using 10 mM EDTA in PBS (pH 7.2), pelleted and then resuspended in Dulbecco's modified PBS (Life Technologies) without Ca^{2+} or Mg^{2+}. Furimazine (Promega) was then added at a 1/100 dilution to a 100-μl cell suspension in a black 96-well plate, and BRET was measured using a PHERAstar FS plate reader (Berthold) equipped with a Venus BRET cube. Acceptor (Venus) and donor (NanoLuc) signals were measured at 535 nm and 475 nm, respectively, and net BRET was calculated by subtracting the acceptor/donor ratio of a donor-only sample from the acceptor/donor ratio of each sample. Readings were taken before and 3–4 min after application of 20 μM 2-AG (Tocris) to activate the CB1R or the eCB sensor.

Tango assay. Plasmids for expression of eCB2.0, eCBmut or CB1R were transfected into a reporter cell line expressing a β-arrestin 2–TEV fusion gene and a tTA-dependent luciferase reporter gene[45]. After transfection (24 h), cells in six-well plates were collected after trypsin digestion and plated in 96-well plates. AEA was applied at final concentrations ranging from 0.01 nM to 10 μM. After luciferase expression (12 h), Bright-Glo (Fluc Luciferase Assay System, Promega) was added to a final concentration of 5 μM, and luminescence was measured using the VICTOR X5 multilabel plate reader (PerkinElmer).

Photometry recording in the dorsolateral striatum in acute mouse brain slices. Adult (>10 weeks of age) male C57BL/6J mice were anesthetized with isoflurane; AAV vectors were injected (300 nl at a rate of 50 nl min^{-1}) into the DLS at the

following coordinates relative to the bregma: anteroposterior (AP), +0.75 mm; ML, ±2.5 mm; and dorsoventral (DV), −3.5 mm. After viral injection, mice received an injection of ketoprofen (5 mg per kg, s.c.), and postoperative care was provided daily until mice regained their preoperative weight. A minimum of 4 weeks following AAV injection, mice were deeply anesthetized with isoflurane and decapitated, and brains were removed and placed in ice-cold cutting solution containing (in mM): 194 sucrose, 30 NaCl, 4.5 KCl, 26 $NaHCO_3$, 1.2 NaH_2PO_4, 10 D-glucose and 1 $MgCl_2$ saturated with 5% CO_2 and 95% O_2. Coronal brain slices (250-µm thickness) were prepared and then incubated at 32 °C for 60 min in artificial cerebrospinal fluid (ACSF) containing (in mM): 124 NaCl, 4.5 KCl, 26 $NaHCO_3$, 1.2 NaH_2PO_4, 10 D-glucose, 1 $MgCl_2$ and 2 $CaCl_2$. After incubation at 32 °C, slices were kept at room temperature until use. Photometry recordings were acquired using an Olympus BX41 upright epifluorescence microscope equipped with a ×40, 0.8-NA water-immersion objective and a FITC filter set. Slices were superfused at 2 ml min^{-1} with ACSF (29–31 °C). A twisted bipolar polyimide-coated stainless-steel stimulating electrode (tip separation of ~200 µm) was placed in the DLS just medial to the corpus callosum and slightly below the tissue surface in a region with visible eCB2.0 or eCBmut fluorescence. Sensors were excited using a 470-nm light-emitting diode (LED) (Thorlabs). Photons passing through a 180-$µm^2$ aperture positioned just lateral to the stimulating electrode were directed to a model D-104 photomultiplier tube (PMT) (Photon Technology International). The PMT output was amplified (gain, 0.1 µA V^{-1}; time constant, 5 ms), filtered at 50 Hz and digitized at 250 Hz using a Digidata 1550B system and Clampex software (Molecular Devices). For each photometry experiment, $GRAB_{eCB}$ signals were measured as discrete trials repeated every 3 min. For each trial, the light exposure duration was 35–45 s to minimize $GRAB_{eCB}$ photobleaching while capturing the peak response and the majority of the decay phase. To evoke an eCB transient, a train of electrical pulses (200–500 µs, 1.0–1.5 mA) was delivered 5 s after initiating $GRAB_{eCB}$ excitation.

Electrophysiology recordings of DSI in acute striatal slices. Adult (5–8 weeks of age) C57BL/6J mice of both sexes were anesthetized with an intraperitoneal injection of 2,2,2-tribromoethanol (Avertin, 500 mg per kg body weight, Sigma-Aldrich), and AAV vectors were injected (300 nl at a rate of 50 nl min^{-1}) into the dorsal striatum region using the following coordinates (relative to the bregma): AP, 1.0 mm; ML, 2.35 mm; and DV, −3.4 mm. Four weeks following AAV injection, acute brain slices were prepared for recording. Mice were anesthetized with isoflurane and decapitated, and brains were extracted and briefly submerged into chilled ACSF containing (in mM): 125 NaCl, 2.5 KCl, 1.25 NaH_2PO_4, 25 $NaHCO_3$, 15 glucose, 2 $CaCl_2$ and 1 $MgCl_2$, oxygenated with 95% O_2 and 5% CO_2 (300–305 mOsm, pH 7.4). Oblique horizontal slices (300-µm thickness) containing dorsal striatum were then prepared using a tissue vibratome (VT1200S, Leica), incubated in chambers containing ACSF at 34 °C for 30 min and then allowed to recover at room temperature for 30 min. After recovery, slices were transferred to a submerged recording chamber perfused with ACSF at a rate of 2–3 ml min^{-1} and a temperature of 30–31 °C. All recording experiments were performed within 5 h of slice recovery. Whole-cell voltage-clamp DSI recordings were made with glass pipettes (3–4 MΩ) filled with a high-chloride internal solution including (in mM): 125.2 CsCl, 10 NaCl, 10 HEPES, 1 EGTA, 2 QX-314 chloride, 0.1 $CaCl_2$, 4 Mg-ATP, 0.3 Na_3-GTP and 8 disodium phosphocreatine (280–290 mOsm, pH 7.3 with CsOH). For DSI recordings, high-Ca^{2+} ACSF (4 mM Ca^{2+}, 0.5 mM Mg^{2+}) was perfused to increase the rate of spontaneous synaptic activity. NBQX (10 µM) and R-CPP (10 µM) were included in the perfusion to block AMPAR-mediated and NMDAR-mediated currents, respectively. Cells were voltage clamped at −70 mV. Access resistance was measured by injection of hyperpolarizing pulses (−5 mV, 100 µs) and was less than 25 MΩ for all recordings, and only cells with a change in access resistance <20% throughout the entire experiment were included in the analysis. sIPSCs were recorded for a baseline of 10 s before depolarization to 0 mV for 5 s and additional recording of sIPSCs for 20 s after depolarization[21]. sIPSC charge (integrated current) was binned every 2 s and normalized to the average of that from the 10 s (five bins) preceding depolarization, and normalized charges before depolarization, after depolarization and 16 s after depolarization were compared. Whole-cell patch-clamp recordings were performed using a MultiClamp 700B (Molecular Devices), monitored with WinWCP (Strathclyde Electrophysiology Software) and analyzed offline using Clampfit 10.0 (Molecular Devices) and custom-made MATLAB (Mathworks) software. Signals were filtered at 2 kHz and digitized at 10 kHz (NI PCIe-6259, National Instruments).

Two-photon imaging in the hippocampus and the BLA in acute mouse brain slices. Adult (6–8 weeks of age) C57BL/6J mice or adult CB1R-P2A-FlpO mice (6–8 weeks of age) of both sexes were anesthetized with an intraperitoneal injection of 2,2,2-tribromoethanol (Avertin, 500 mg per kg body weight, Sigma-Aldrich), and AAV vectors were injected (400 nl at a rate of 46 nl min^{-1}) into the hippocampal CA1 region (coordinates: AP, −1.8 mm relative to the bregma; ML, ±1.0 mm relative to the bregma; and DV, −1.2 mm relative to the brain surface) or the BLA region (coordinates: AP, −1.40 mm relative to the bregma; ML, −3.10 mm relative to the bregma; and DV, −4.20 mm relative to the brain surface). At least 4 weeks following AAV injection, mice were deeply anesthetized with an intraperitoneal injection of 2,2,2-tribromoethanol and decapitated, and brains were removed and placed in ice-cold cutting solution containing (in mM): 110 choline chloride, 2.5 KCl, 0.5 $CaCl_2$, 7 $MgCl_2$, 1 NaH_2PO_4, 1.3 sodium ascorbate, 0.6 sodium pyruvate, 25 $NaHCO_3$ and 25 glucose saturated with 5% CO_2 and 95% O_2. Coronal brain slices (300-µm thickness) were prepared and incubated at 34 °C for approximately 40 min in modified ACSF containing (in mM): 125 NaCl, 2.5 KCl, 2 $CaCl_2$, 1.3 $MgCl_2$, 1 NaH_2PO_4, 1.3 sodium ascorbate, 0.6 sodium pyruvate, 25 $NaHCO_3$ and 25 glucose saturated with 5% CO_2 and 95% O_2; 75 mM K^+ ACSF instead contained 52.5 mM NaCl and 75 mM KCl. Two-photon imaging was performed using an FV1000MPE 2P microscope (Olympus) equipped with a ×25, 1.05-NA water-immersion objective and a mode-locked Mai Tai Ti:Sapphire laser (Spectra-Physics). Slices were superfused with modified ACSF (32–34 °C) at a rate of 4 ml min^{-1}. A 920-nm laser was used to excite the eCB2.0 sensor, and fluorescence was collected using a 495–540-nm filter. For electrical stimulation, a bipolar electrode (WE30031.0A3, MicroProbes for Life Science) was positioned near the stratum radiatum layer in the CA1 region using fluorescence guidance. Fluorescence imaging and electrical stimulation were synchronized using an Arduino board with custom-written software. The stimulation voltage was 4–6 V, and the pulse duration was 1 ms. Drugs were applied to the imaging chamber by perfusion at a flow rate of 4 ml min^{-1}.

Fiber photometry recording of eCB signals in the basolateral amygdala. Adult (10–12 weeks of age) C57BL/6J mice of both sexes were anesthetized, and 300 nl of either a 10:1 mixture of AAV-hSyn-eCB2.0 and AAV-hSyn-mCherry, a 10:1 mixture of AAV-hSyn-eCBmut and AAV-hSyn-mCherry or a 1:1 mixture of AAV-hSyn-eCB2.0 and AAV-CaMKII-ChRmine-mScarlet was injected using a glass pipette and a Picospritzer III microinjection system (Parker Hannifin) into the right BLA using the following coordinates: AP, −1.78 mm relative to the bregma; ML, −3.30 mm relative to the bregma; and DV, −4.53 mm relative to the brain surface. After injection, a fiber (200-µm diameter, 0.37 NA, Inper) was implanted at the same location and secured using resin cement (3M). A head bar was also mounted onto the skull using resin cement.

At least 14 d after surgery, photometry recording was performed using a commercial photometry system (FP3001 or FP3002, Neurophotometrics). A patch cord (0.37 NA, Doric Lenses) was attached to the photometry system and to the fiber secured in the mouse brain. A 470-nm LED (160 µW) was used to excite $GRAB_{eCB}$ sensors, a 405-nm LED (50 µW) was used for excitation to obtain the isosbestic signal, and a 560-nm LED (25 µW) was used to excite mCherry.

For optogenetic manipulation experiments, mice were tested under head restraint in a sound-attenuated box. A 635-nm laser (1–3 mW) on the FP3002 system was used for optogenetic stimulation; 40-Hz (5 ms per pulse) 1-s laser stimulation was delivered through the same fiber as that for photometry recording with an interval of 90–120 s between trials. For foot shock experiments, mice were allowed to move freely in a Habitest shock box (Coulbourn Instruments) inside a lighted soundproof behavior box. The FreezeFrame software program was used to apply triggers to the shock generator (Coulbourn Instruments). Five 2-s pulses of electricity at an intensity of 0.7 mA were delivered to the shock box with an interval of 90–120 s between trials. Photometry data were acquired with Bonsai 2.3.1 or 2.6.2 software (Bonsai) and were exported to MATLAB for further analysis. Photometry signals and behavioral events were aligned based on an analog TTL signal generated by the Bpod. To correct for photobleaching of fluorescence signals (baseline drift), a bi-exponential curve was fit to the raw fluorescence trace and subtracted as follows:

$$F_{\text{raw fit}} = \text{fit}(\text{timestamp}, F_{\text{raw}}, \text{'exp 2'})$$

$$F_{\text{raw correction}} = \frac{F_{\text{raw}} - F_{\text{raw fit}}}{F_{\text{raw fit}}}.$$

After baseline drift correction, fluorescence signals were z scored relative to the mean and s.d. of the signals in a time window −5 to 0 s relative to stimulus onset.

After photometry recording, animals were deeply anesthetized and perfused with PBS followed by 4% paraformaldehyde (PFA) in PBS. Brains were removed, fixed in 4% PFA overnight and then dehydrated with 30% sucrose in PBS for 24 h. Brain slices were cut using a Leica SM2010R microtome (Leica Biosystems). Floating brain slices were blocked at room temperature for 2 h with a blocking solution containing 5% (wt/vol) BSA and 0.1% Triton X-100 in PBS and then incubated at 4 °C for 24 h in PBS containing 3% BSA, 0.1% Triton X-100 and the following primary antibodies: chicken anti-GFP (1:1,000, Aves, GFP-1020) and rabbit anti-RFP (1:500, Rockland, 600-401-379). The next day, slices were rinsed three times in PBS and incubated in PBS with DAPI (5 µg ml^{-1}, Invitrogen, D1306) and the following secondary antibodies at 4 °C for 24 h: Alexa Fluor 488 donkey anti-chicken (1:250, Jackson ImmunoResearch, 703-545-155) and Alexa Fluor 568 donkey anti-rabbit (1:250, Invitrogen, A10042). Confocal images were captured using an LSM 780 confocal microscope (Zeiss).

Behavioral tests in mice expressing eCB2.0 in the basolateral amygdala. Adult (10–12 weeks of age) C57BL/6J mice of both sexes were anesthetized, and 300 nl of either AAV-hSyn-eCB2.0 or AAV-CAG-GFP was injected into the BLA bilaterally, similar to the procedure for the BLA fiber photometry recording experiment.

The same cohort of mice was subjected to various behavioral tests at least 14 d after surgery in the following order: open-field test, elevated plus maze test and fear conditioning. Mice were handled for 2 d for 10 min each day before experiments.

Open-field test. The open-field test was performed in a non-transparent square box (42.5 cm × 42.5 cm × 40 cm), which was enclosed in a sound-attenuating chamber illuminated with a house light. Animals were placed in one corner of the arena at the start of the test. Mice were allowed to explore the arena for 5 min while their behavior was videotaped at 5 Hz using a Logitech C930e camera. The arena was thoroughly cleaned with 70% ethanol between subjects. Data were analyzed using EthoVision XT 5.1 software (Noldus Information Technology; RRID, SCR_000441). The center zone was set to 21 × 21 cm in the middle of the arena.

Elevated plus maze test. The elevated plus maze has two open arms without walls (30 cm long and 5 cm wide) and two arms enclosed by 15.25-cm-high non-transparent walls. The arms were connected by a central platform (5 × 5 cm) with identical (open or closed) arms located opposite from each other. The maze was 50 cm above the floor. At the start of the session, animals were first placed in the center zone with their heads oriented to a closed arm. Mice were allowed to explore the maze for 10 min while their behavior was videotaped at 30 Hz using a Logitech C920 camera. The maze was thoroughly cleaned with 70% ethanol between subjects. Data were analyzed using EthoVision XT 5.1 software.

Auditory fear conditioning. We followed standard procedures for conventional auditory fear conditioning[69–71]. Briefly, on day 1 (habituation), mice were handled and habituated to a conditioning cage, which was a mouse test cage (18 cm × 18 cm × 30 cm) with an electrifiable floor connected to a H13-15 shock generator (Coulbourn Instruments). The test cage was placed inside a sound-attenuating cabinet (H10-24A, Coulbourn Instruments) and illuminated with white light. During habituation, five repetitions of a sound (conditioned stimulus (CS); 7-kHz pure tone, 70 dB, 30 s in duration) were presented at 60–90 s intertrial intervals.

On day 2 (conditioning), mice were placed back into the test cage inside the white light-illuminated cabinet as on day 1 and received five presentations of the CS, each of which co-terminated with a foot shock (unconditioned stimulus; 2 s in duration, 0.7 mA). Intertrial intervals were 60–90 s. Before each habituation and conditioning session, the test cage was wiped with 70% ethanol.

On day 3, the test for fear memory (retrieval) was performed in a novel context, in which mice were exposed to two presentations of the CS, with an interval of 115 s. The novel context was a cage with a different shape (22 cm × 22 cm × 21 cm) and floor texture than the conditioning cage and was illuminated with infrared light. Before each use, the floor and walls of the cage were wiped clean with 0.5% acetic acid to make the scent distinct from that of the conditioning cage.

Animal behavior was videotaped at 3.7 Hz with a monochrome CCD camera (Panasonic, WV-BP334). FreezeFrame software (Coulbourn Instruments) was used to control the delivery of both tones and foot shocks. Freezing behavior was analyzed with FreezeFrame software.

Two-photon in vivo imaging. Adult (100–150 d in age) C57BL/6J mice of both sexes were used for these experiments. Mice were anesthetized, and a mixture of AAV1-Syn-NES-jRGECO1a-WPRE-SV40 and either AAV9-hSyn-eCB2.0 or AAV9-hSyn-eCBmut (300–400 nl each, full titer) was injected into the right hippocampal CA1 region at the following coordinates relative to the bregma using a Hamilton syringe: AP, 2.3 mm; ML, 1.5 mm; and DV, −1.35 mm. After viral injection, a stainless-steel cannula with an attached coverglass was implanted over the hippocampus as described previously[72,73], and a stainless-steel head bar was attached. A chronic bipolar wire electrode (tungsten, 0.002', tip separation of 0.5 mm, A-M Systems) was implanted into the left ventral hippocampus at the following coordinates relative to the bregma as previously described[74]: AP, 3.2 mm; ML, 2.7 mm; and DV, −4.0 mm. Head-fixed mice running on a linear treadmill with a 2-m-long cueless belt were imaged using a resonant scanning 2P microscope (Neurolabware) equipped with a pulsed IR laser tuned to 1,000 nm (Mai Tai, Spectra-Physics), GaAsP PMT detectors (H11706P-40, Hamamatsu) and a ×16, 0.8-NA water-immersion objective (Nikon). Two-photon image acquisition and treadmill speed were controlled and monitored using a Scanbox (Neurolabware). Bipolar electrodes were recorded using a model 1700 differential amplifier (A-M Systems). Seizures were elicited by applying electric stimulation above the seizure threshold by 150 µA of current delivered in 1-ms biphasic pulses at 60 Hz for 1 s using a model 2100 constant-current stimulator (A-M Systems). Following in vivo recordings, mice were anesthetized with isoflurane followed by an intraperitoneal injection of a mixture of ketamine (100 mg per kg body weight) and xylazine (10 mg per kg body weight) in saline. Mice were transcardially perfused with 0.9% NaCl for 1 min followed by 4% PFA and 0.2% picric acid in 0.1 M phosphate buffer. Brains were removed, post-fixed in the same fixative solution for 24 h at 4 °C and then sliced on a VTS1200 vibratome (Leica Biosystems). Sections were then washed and mounted using VECTASHIELD (Vector Laboratories). Confocal images were acquired using an LSM 710 imaging system equipped with a ×20, 0.8-NA objective (Zeiss).

Data processing. *Confocal imaging.* Data for 96-well plate imaging were collected and analyzed using Harmony high-content imaging and analysis software (PerkinElmer). In brief, membrane regions were selected as ROI and the green fluorescence channel (that is, the sensor) was normalized to the red fluorescence channel corresponding to mCherry-CAAX (G/R). The $\Delta F/F_0$ values were then calculated using the formula $(G/R_{drug} - G/R_{baseline})(G/R_{baseline})^{-1}$. For 12-mm coverslip imaging, data were collected using NIS-Element software (Nikon) and analyzed using ImageJ software (National Institutes of Health). The calculation for $\Delta F/F_0$ was carried out using the formula $(F_t - F_0)F_0^{-1}$, where F_0 represents baseline fluorescence. Data were plotted using OriginPro 2020 (OriginLab).

Slice photometry and two-photon imaging. For slice photometry, $GRAB_{eCB}$ signals were calculated with the formula $\Delta F/F_0$ by averaging the PMT voltage (V) for a period of 1 s just before electrical stimulation (F_0) and then calculating $V(F_0)^{-1} - 1$ for each digitized data sample. The decay phase was fitted with a single exponential, accounting for a sloping baseline. Rise $t_{1/2}$ was calculated in Prism version 8.3 (GraphPad) by fitting the rising phase of the signal with an asymmetrical logistic curve. Photometry sweeps were exported to Microsoft Excel 2016 to calculate normalized $\Delta F/F_0$ traces and peak $\Delta F/F_0$ values. For 2P imaging of slices, data were collected using FV10-ASW software (Olympus) and analyzed using ImageJ. The $\Delta F/F_0$ values were calculated using the formula $(F_t - F_0)F_0^{-1}$, where F_0 represents baseline fluorescence. Data were plotted using OriginPro 2020.

Fiber photometry in mice during foot shock. Fiber photometry data were analyzed offline using Excel or MATLAB software (MathWorks) and plotted using OriginPro 2020.

Two-photon imaging in mice during locomotion and seizure. Imaging data were processed and analyzed using Python scripts. To analyze single-cell responses, videos were initially corrected for motion using rigid translation, followed by non-rigid correction ('HiddenMarkov2D') using the SIMA package[75]. Binary ROI were selected using a semi-automated approach. For the initial automated detection, videos were divided into segments consisting of 100 frames each; the average intensity projection of each segment was then computed, and the resulting resampled movie was used for detection. In sessions with electric stimulation, only the baseline period (that is, before stimulation) was used for segmentation. The 'PlaneCA1PC' method of SIMA was run on the inverted resampled video, which resulted in detection of hollow cell nuclei. These ROI were then filtered based on size, and binary dilation was performed to include the cytoplasm around the nuclei. Next, ROI were detected in the non-inverted resampled video and filtered based on size; those samples that did not overlap with existing ROI were added to the set. ROI outside the stratum pyramidale layer were excluded. Fluorescence intensity traces were then extracted for each ROI by averaging the included pixel intensities within each frame. For analyzing run responses, only sessions with no electric stimuli were included, and signals were pulled from the motion-corrected movies. These raw traces were then processed following standard steps for obtaining $\Delta F/F_0$ traces, with a modified approach for determining the time-dependent baseline. A third-degree polynomial was fit to the trace after applying temporal smoothing, removing peaks (detected using continuous wavelet transform with scipy.signal), eliminating periods of running and ignoring the beginning and end of the recording. The calculated polynomial was then used as a baseline. z-scored traces were obtained after determining the s.d. of each cell's baseline and excluding events exceeding 2 s.d. in two iterations.

To analyze spreading activity, only sessions with an electric stimulus that triggered an electrographic seizure and a spreading wave were included. Segmentation was performed based on motion-corrected baseline segments of the recordings, and signals were pulled from non-motion-corrected videos, as image-based motion correction was not feasible during seizures. The $\Delta F/F_0$ traces were obtained using a constant baseline determined by averaging pre-stimulus segments of the traces. To analyze changes in average fluorescence intensity, a single large ROI was manually drawn to include the cell bodies within the pyramidal layer, and $\Delta F/F_0$ traces were obtained and processed as described above. Event-triggered averages were calculated after automatically detecting frames with running onsets and stops using criteria that were fixed across all sessions. The average was computed in two steps; first, events were averaged by cell, and then cells were averaged by sensor (for example, eCB2.0 or eCBmut). Decay time constants were computed as the parameter of a second-degree polynomial fit after a log transform on the trace following the peak of the stop-triggered average trace. Rise times were determined between the frame in which the start-triggered average signal first reached 90% of the range between baseline and peak and the last frame before the signal dropped below 10% of the range. To determine the speed and direction of spreading waves, the peak time of the wave was determined in each session by inspecting the average $\Delta F/F_0$ trace (including all cells). Next, the relative peak location (Δt) of the $\Delta F/F_0$ trace of each cell in the trace including 200 frames (12.8 s) before and after the wave peak was determined. Finally, two linear (that is, 1D) fits were determined using x and y centroid coordinates of each ROI ($\Delta t \approx x$, $\Delta t \approx y$). The 2D speed was then computed from the slopes of the two 1D fits. The direction was determined by computing the unity vector from the starting point

to the end point of the fits between 3 s before and after the wave peak. The average speed was obtained by averaging the speed of individual sessions, and the average direction was obtained from the sum of the unity vectors of individual sessions. Data were plotted using Python and OriginPro 2020.

Statistical analysis. Group data were analyzed using Student's *t*-test, one-way ANOVA, two-way ANOVA, Mann–Whitney test or Wilcoxon matched-pairs signed-rank tests. $^{*}P < 0.05$; $^{**}P < 0.01$; $^{***}P < 0.001$; and NS, $P > 0.05$. Exact *P* values are specified in the legends.

Reporting Summary. Further information on research design is available in the Nature Research Reporting Summary linked to this article.

Data availability

Plasmids for expressing eCB2.0 and eCBmut used in this study have been deposited to Addgene (164604–164612). Source data are provided with this paper.

Code availability

The SIMA package used for in vivo 2P imaging analysis is available at https://github.com/losonczylab/sima. Custom MATLAB and Arduino codes are available at https://github.com/hbhzshengao/dsi_events_analysis and https://github.com/hbhzshengao/2p_imaging_stim.

References

67. Masuho, I. et al. Distinct profiles of functional discrimination among G proteins determine the actions of G protein-coupled receptors. *Sci. Signal.* **8**, ra123 (2015).
68. Hollins, B., Kuravi, S., Digby, G. J. & Lambert, N. A. The C-terminus of GRK3 indicates rapid dissociation of G protein heterotrimers. *Cell. Signal.* **21**, 1015–1021 (2009).
69. Li, H. et al. Experience-dependent modification of a central amygdala fear circuit. *Nat. Neurosci.* **16**, 332–339 (2013).
70. Penzo, M. A. et al. The paraventricular thalamus controls a central amygdala fear circuit. *Nature* **519**, 455–459 (2015).
71. Yu, K. et al. The central amygdala controls learning in the lateral amygdala. *Nat. Neurosci.* **20**, 1680–1685 (2017).
72. Kaifosh, P., Lovett-Barron, M., Turi, G. F., Reardon, T. R. & Losonczy, A. Septo-hippocampal GABAergic signaling across multiple modalities in awake mice. *Nat. Neurosci.* **16**, 1182–1184 (2013).
73. Lovett-Barron, M. et al. Dendritic inhibition in the hippocampus supports fear learning. *Science* **343**, 857–863 (2014).
74. Farrell, J. S. et al. Postictal behavioural impairments are due to a severe prolonged hypoperfusion/hypoxia event that is COX-2 dependent. *eLife* **5**, e19352 (2016).
75. Kaifosh, P., Zaremba, J. D., Danielson, N. B. & Losonczy, A. SIMA: Python software for analysis of dynamic fluorescence imaging data. *Front. Neuroinform.* **8**, 80 (2014).

Acknowledgements

This work was supported by the National Natural Science Foundation of China (31925017 and 31871087), the Beijing Municipal Science & Technology Commission (Z181100001318002 and Z181100001518004), the NIH BRAIN Initiative (1U01NS113358), the Shenzhen-Hong Kong Institute of Brain Science (NYKFKT2019013), the Science Fund for Creative Research Groups of the National Natural Science Foundation of China (81821092) and grants from the Peking-Tsinghua Center for Life Sciences and the State Key Laboratory of Membrane Biology at Peking University School of Life Sciences (Y.L.); the NIAAA (ZIA AA000416) (D.M.L.); the NIH BRAIN Initiative (1U01NS113358) (J. Ding); the NIH (R01MH101214 and R01NS104944) (B.L.); the American Epilepsy Society (postdoctoral fellowship) and the NIH (K99NS117795) (B.D.); the Canadian Institutes for Health Research (postdoctoral fellowship) (J.S.F.); and the NIH (NS99457) (I.S.). We thank members and alumni of the Li laboratory for helpful discussions. We thank Y. Rao at PKU for use of the 2P microscope, Y. Xue at PKU Health Science Center for assistance with the Δ-9-THC experiment and X. Lei at PKU-CLS and the National Center for Protein Sciences at Peking University in Beijing, China, for support and assistance with the Opera Phenix high-content screening system and imaging platform.

Author contributions

Y.L. conceived the project. A.D., K.H., H.L.P., R.C., H.W. and J. Duan performed experiments related to developing, optimizing and characterizing sensors in cultured HEK293T cells and neurons. D.J.L. performed surgery and photometry recording experiments related to the validation of the sensor in DLS brain slices under the supervision of D.M.L. A.D. performed the surgery and 2P imaging in hippocampal brain slices. E.A. performed the surgery and electrophysiological recordings in striatal brain slices under the supervision of J. Ding. W.G. performed fiber photometry recordings in freely moving mice during foot shock under the supervision of B.L. B.D. and J.S.F. performed in vivo 2P imaging in the hippocampus in mice during running and seizure under the supervision of I.S. All authors contributed to data interpretation and analysis. A.D. and Y.L. wrote the manuscript with input from other authors.

Competing interests

Y.L. and H.W. have filed patent applications (international patent no. PCT/CN2018/107533), the value of which might be affected by this publication. The remaining authors declare no competing interests.

Additional information

Extended data is available for this paper at https://doi.org/10.1038/s41587-021-01074-4.

Supplementary information The online version contains supplementary material available at https://doi.org/10.1038/s41587-021-01074-4.

Correspondence and requests for materials should be addressed to Yulong Li.

Peer review information *Nature Biotechnology* thanks Daniele Piomelli, Pablo Castillo and the other, anonymous, reviewer(s) for their contribution to the peer review of this work.

Reprints and permissions information is available at www.nature.com/reprints.

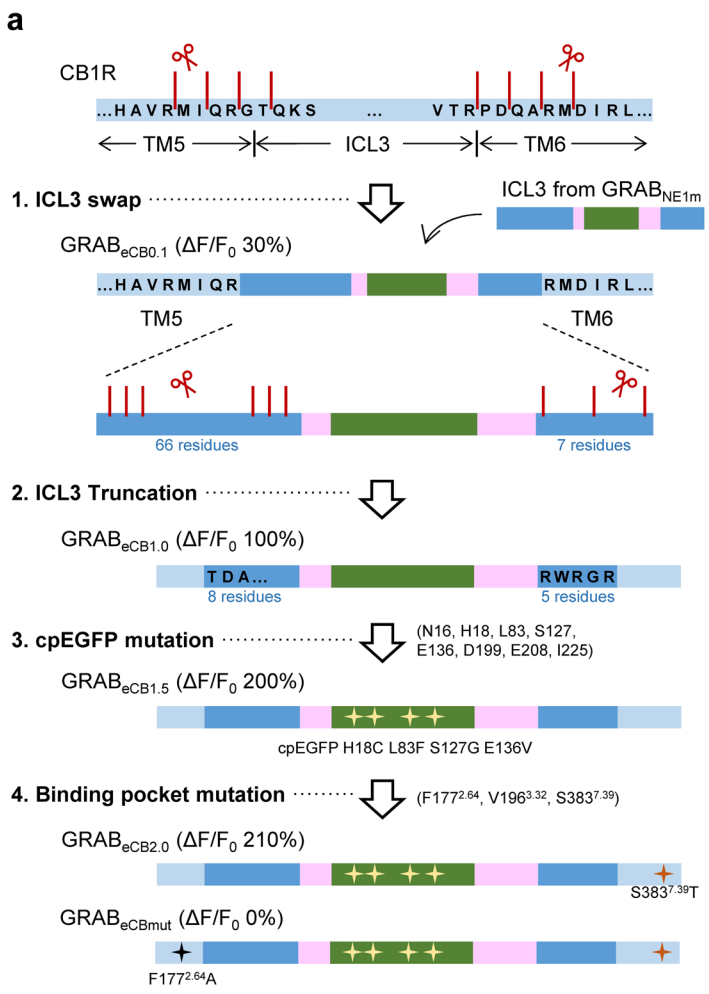

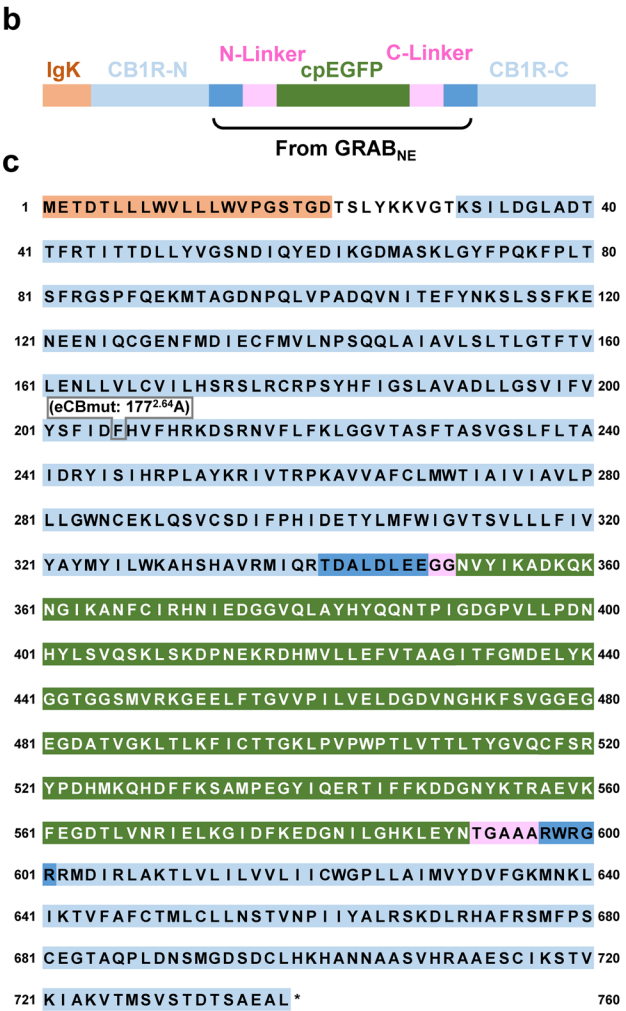

Extended Data Fig. 1 | Strategy for optimizing and screening the GRAB$_{eCB}$ sensors. a, A flowchart showing the development process of the eCB2.0 sensor. Responses to 10 μM 2-AG of candidate sensors were shown alongside each step. **b**, Schematic diagram depicting the structure of the GRAB$_{eCB2.0}$ sensor. The IgK leader sequence and the sequence derived from GRAB$_{NE}$ are shown. **c**, Amino acids sequence of the eCB2.0 sensor. The phenylalanine residue at position 177$^{2.64}$ in the CB1R was mutated to an alanine to generate the eCBmut sensor (indicated by the gray box). Note that the numbering used in the figure corresponds to the start of the IgK leader sequence.

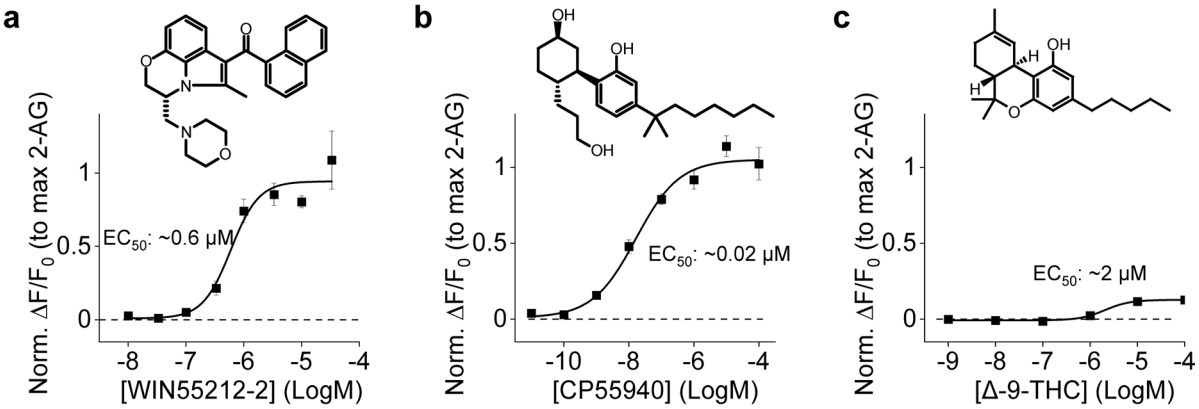

Extended Data Fig. 2 | Dose–response curves of GRAB$_{eCB2.0}$ to synthetic CB1R agonists and the phytocannabinoid Δ-9-THC. a, Dose–response curve of eCB2.0 to WIN55212-2; n = 3 wells each, mean ± s.e.m. **b**, Dose–response curve of eCB2.0 to CP55940; n = 3 wells each, mean ± s.e.m. **c**, Dose–response curve of eCB2.0 to Δ-9-THC; n = 3 wells each, mean ± s.e.m.

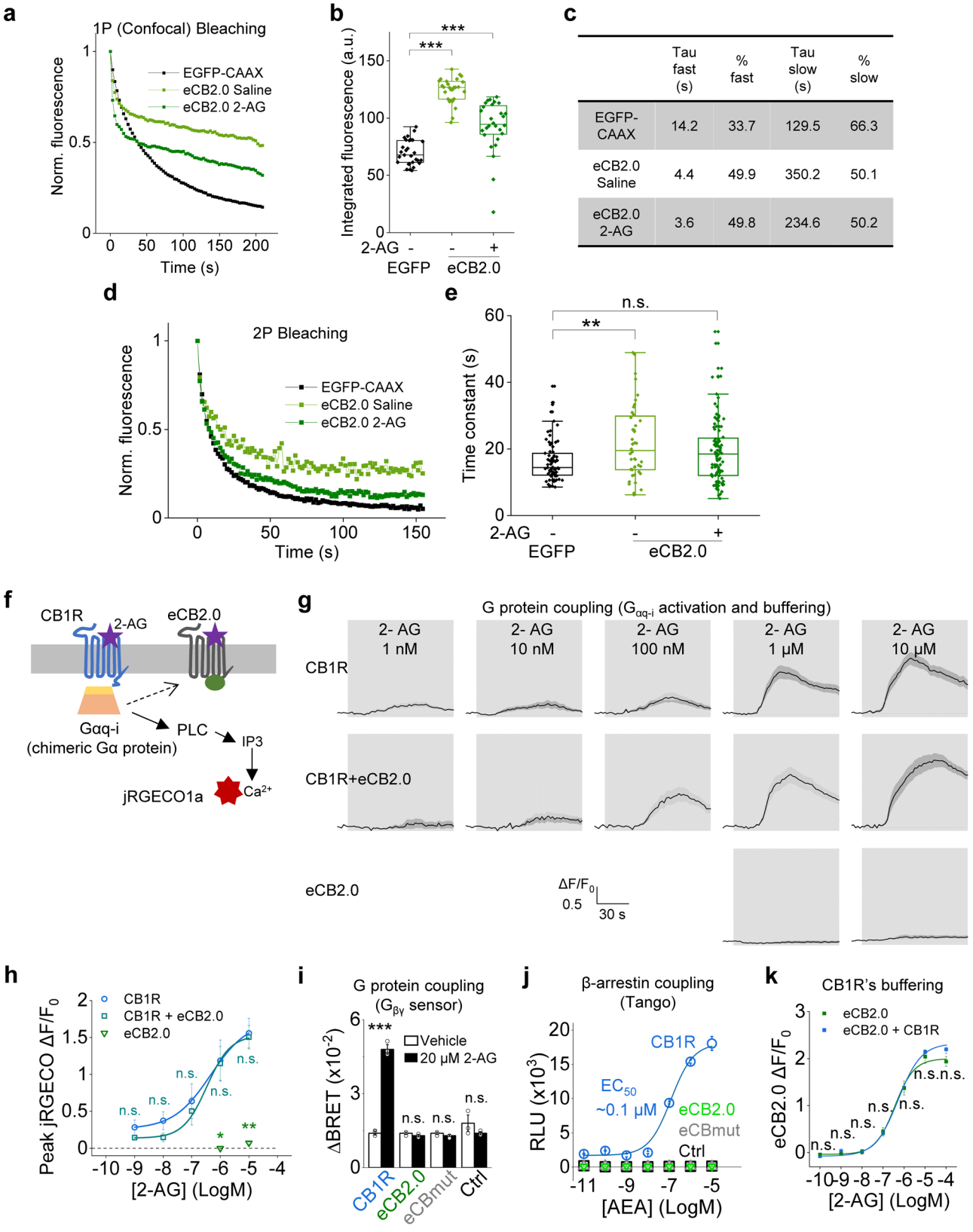

	Tau fast (s)	% fast	Tau slow (s)	% slow
EGFP-CAAX	14.2	33.7	129.5	66.3
eCB2.0 Saline	4.4	49.9	350.2	50.1
eCB2.0 2-AG	3.6	49.8	234.6	50.2

Extended Data Fig. 3 | See next page for caption.

Extended Data Fig. 3 | Photostability and intracellular signaling couplings of GRAB$_{eCB2.0}$ sensor. a, Normalized fluorescence of EGFP-CAAX and eCB2.0 (in the absence and presence of 2-AG) in HEK293T cells during 1P (confocal) bleaching. **b**, Integrated fluorescence of EGFP-CAAX and eCB2.0 (in the absence and presence of 2-AG) shown in a; n = 29, 27, 28 cells from 3 cultures. Boxes show the first and third quartiles as well as the median (line), and the whiskers extend to the most extreme data point that is no more than 1.5× the interquartile range from the box. Two-tailed Mann-Whitney tests were performed: P = 1.44E-10 (between EGFP and eCB2.0 in saline) and 1.37E-6 (between EGFP and eCB2.0 with 2-AG). **c**, Fast and slow time constants and slow component amplitudes of EGFP-CAAX and eCB2.0 (in the absence and presence of 2-AG) traces fit by double exponentials. **d**, Normalized fluorescence of EGFP-CAAX and eCB2.0 (in the absence and presence of 2-AG) in HEK293T cells during 2P bleaching. **e**, Time constants of EGFP-CAAX and eCB2.0 (in the absence and presence of 2-AG) traces fit by single exponentials; n = 79, 48, 104 cells from 3 cultures. Boxes show the first and third quartiles as well as the median (line), and the whiskers extend to the most extreme data point that is no more than 1.5× the interquartile range from the box. Two-tailed Mann-Whitney tests were performed: P = 0.0049 (between EGFP and eCB2.0 in saline) and 0.0581 (between EGFP and eCB2.0 with 2-AG). **f**, Schematic diagram depicting the strategy for measuring G protein activation using the chimeric $G\alpha_{q-i}$ protein. **g**, Representative traces showing the jRGECO1a responses to 2-AG perfusion in cells expressing CB1R, CB1R + eCB2.0 or eCB2.0. **h**, Dose-response curves of peak jRGECO1a $\Delta F/F_0$ measured in cells expressing CB1R, CB1R + eCB2.0, or eCB2.0; n = 4, 4 and 3 cultures, mean ± s.e.m. Two concentrations of 2-AG were used for eCB2.0 expressed cells. Two-tailed Student's t tests were performed: P = 0.2392, 0.1455, 0.6711, 0.9191 and 0.8371 (between CB1R and CB1R + eCB2.0); P = 0.0156 and 0.0015 (between CB1R and eCB2.0). **i**, G protein coupling was measured using a BRET $G_{\beta\gamma}$ sensor in cells expressing CB1R, eCB2.0, or eCBmut; n = 3 experiments, mean ± s.e.m. Two-tailed Student's t tests were performed: P = 3.84E-05, 0.4082, 0.0699 and 0.2961. **j**, β-arrestin coupling was measured using the Tango assay in cells expressing CB1R, eCB2.0, or eCBmut; n = 3 wells each, mean ± s.e.m. **k**, Dose-response curves of eCB2.0 to 2-AG measured in cells expressing eCB2.0 or eCB2.0 + CB1R; n = 3 wells each, mean ± s.e.m. Two-tailed Student's t tests were performed: P = 0.3036, 0.3231, 0.7697, 0.7900, 0.9723, 0.5482 and 0.1383. ***, $p < 0.001$; **, $p < 0.01$; *, $p < 0.05$; n.s., not significant.

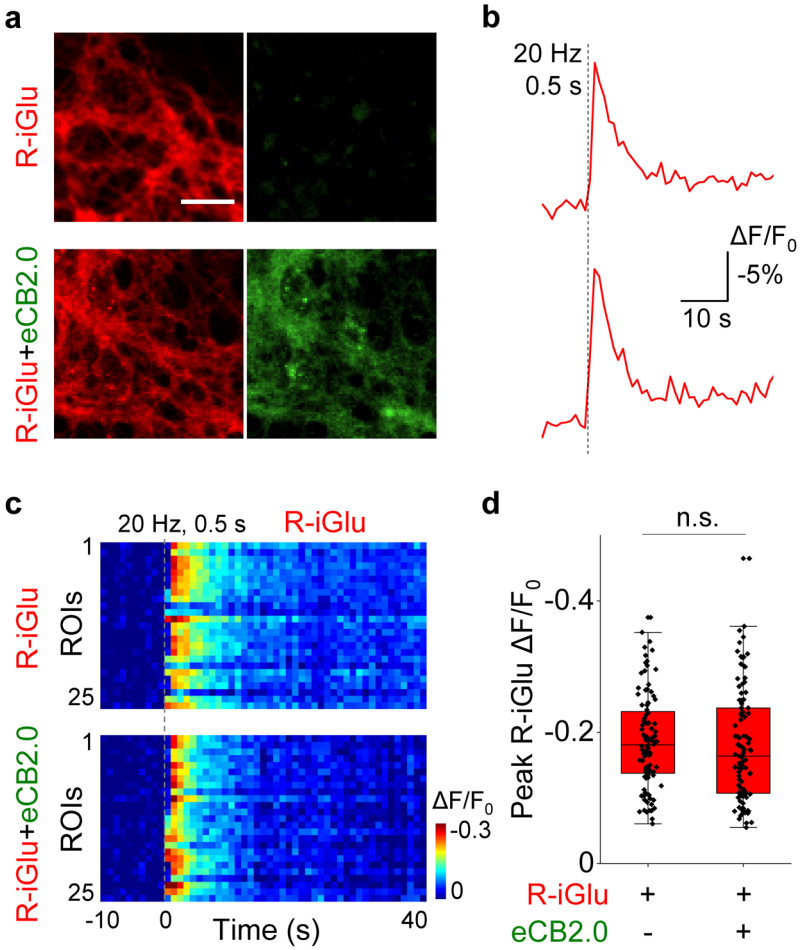

Extended Data Fig. 4 | Expression of GRAB$_{eCB2.0}$ has no significant effect on electrically evoked glutamate release in cultured neurons. a, Fluorescence microscopy images of neurons expressing R^{ncp}-iGluSnFR (upper) and neurons co-expressing R^{ncp}-iGluSnFR and eCB2.0 (bottom). Similar results were observed for more than 20 neurons. Scale bar, 30 μm. **b**, Example traces showing the electrical stimulation evoked glutamate signals. **c**, Pseudocolor change in R^{ncp}-iGluSnFR fluorescence in neurons expressing R^{ncp}-iGluSnFR (upper) and co-expressing R^{ncp}-iGluSnFR and eCB2.0 (bottom) before and after the electrical stimulation. Shown are 25 regions of interest (ROIs) in one culture each. **d**, Summary of peak R^{ncp}-iGluSnFR $\Delta F/F_0$ measured in neurons expressing R^{ncp}-iGluSnFR (upper) or co-expressing R^{ncp}-iGluSnFR and eCB2.0 (bottom); n = 100 ROIs from 4 cultures each. Boxes show the first and third quartiles as well as the median (line), and the whiskers extend to the most extreme data point that is no more than 1.5× the interquartile range from the box. Two-tailed Mann-Whitney test was performed: P = 0.2564. n.s., not significant.

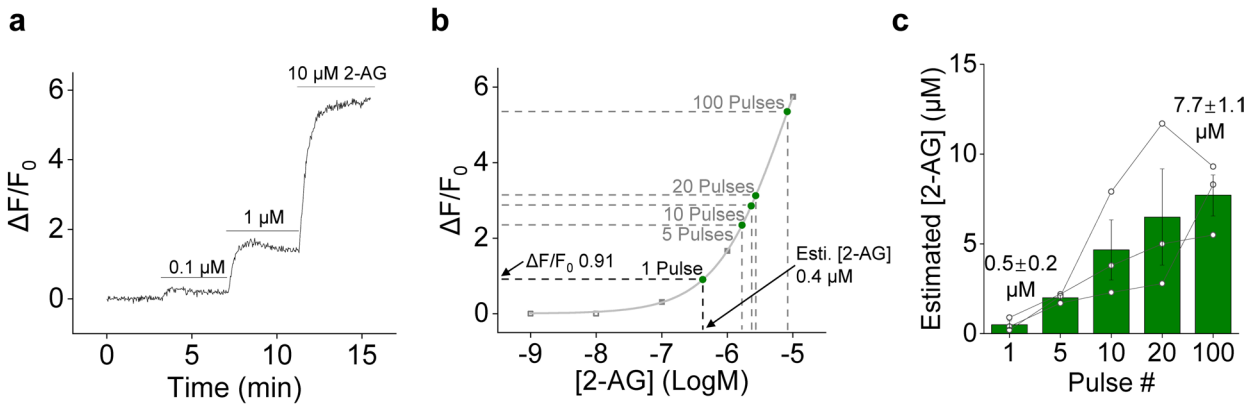

Extended Data Fig. 5 | Estimated concentrations of electrically evoked 2-AG release in cultured neurons. a, An example trace of $\Delta F/F_0$ measured in eCB2.0 expressed neurons; the indicated concentrations of 2-AG were applied. **b**, An example dose-response curve measured in neurons expressing eCB2.0. eCB2.0 signals evoked by 1–100 electrical pulses at 20 Hz and corresponding estimated 2-AG concentrations were indicated (green dots). **c**, Summary of estimated 2-AG release concentrations evoked by 1–100 electrical pulses at 20 Hz; n = 3 cultures, mean ± s.e.m.

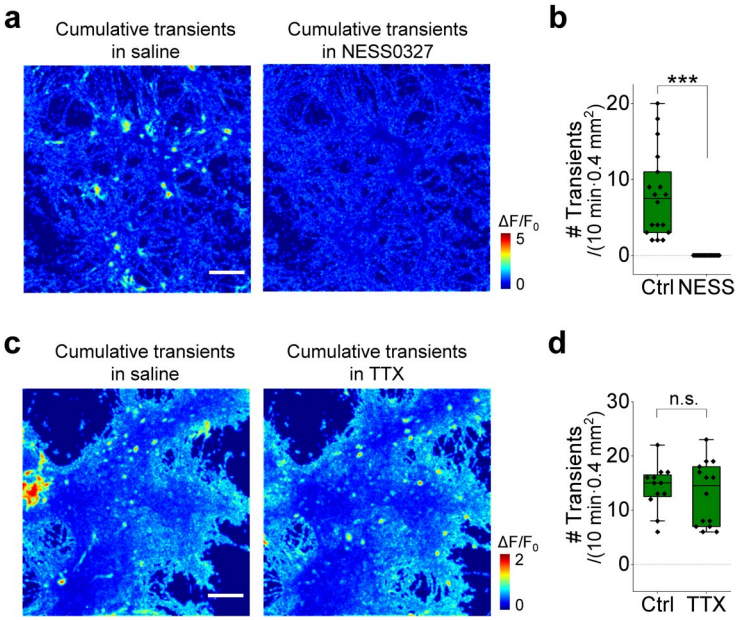

Extended Data Fig. 6 | Spontaneous eCB transients in cultured neurons are sensitive to the CB1R neutral antagonist but not the action potential blocker. **a**, Cumulative transient change in eCB2.0 fluorescence measured during 20 mins of recording in the absence (left) or presence (right) of 1 μM NESS0327. Pseudocolor images were calculated as the average temporal projection subtracted from the maximum temporal projection. Similar results were observed for 3 cultures. Scale bar, 100 μm. **b**, Summary of the frequency of transient changes in eCB2.0 fluorescence measured in saline (Ctrl) and after NESS0327 application; n = 18 & 18 sessions from 3 cultures with 10-min recording/session. Boxes show the first and third quartiles as well as the median (line), and the whiskers extend to the most extreme data point that is no more than 1.5× the interquartile range from the box. Two-tailed Student's t test was performed: P = 1.68E-5. **c**, Cumulative transient change in eCB2.0 fluorescence measured during 20 mins of recording in the absence (left) or presence (right) of 1 μM TTX. Pseudocolor images were calculated as the average temporal projection subtracted from the maximum temporal projection. Similar results were observed for 3 cultures. Scale bar, 100 μm. **d**, Summary of the frequency of transient changes in eCB2.0 fluorescence measured in saline (Ctrl) and after TTX application; n = 12 & 14 sessions from 3 cultures with 10-min recording/session. Boxes show the first and third quartiles as well as the median (line), and the whiskers extend to the most extreme data point that is no more than 1.5× the interquartile range from the box. Two-tailed Student's t test was performed: P = 0.5972. ***, $p < 0.001$; n.s., not significant.

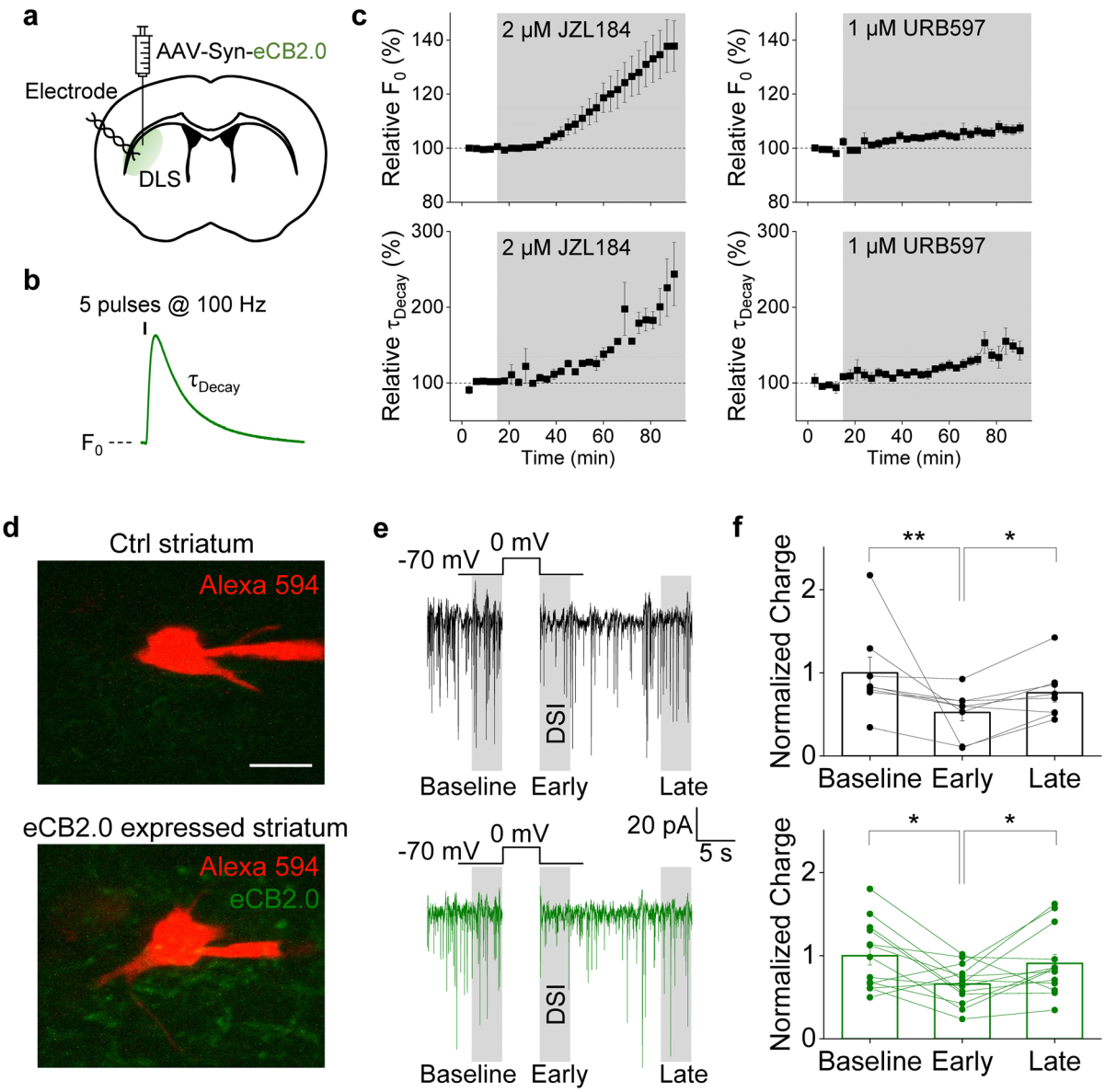

Extended Data Fig. 7 | Detection of 2-AG, AEA, and DSI in GRAB$_{eCB2.0}$ expressed acute striatal slices. a, Schematic diagram depicting the strategy for virus injection in DLS, followed by the preparation of acute brain slices used for electrical stimulation and recording. **b**, Schematic diagram depicting the quantification of F_0 and decay time constant of the evoked eCB2.0 signal. **c**, Quantification of relative F_0 and decay time constant of evoked eCB2.0 signals before and after JZL184 or URB597 treatment. n = 3 slices, mean ± s.e.m. **d**, Fluorescence microscopy images of control and eCB2.0 expressed striatal slices. Recorded MSN neurons were loaded with Alexa 594. Similar results were observed for more than 10 neurons. Scale bar, 10 μm. **e**, Depolarizing neurons in control and eCB2.0 expressed striatum caused similar depression on sIPSC. Three shadow regions correspond to baseline, early and late in c. **f**, Summary of normalized charge recorded in MSNs in control and eCB2.0 expressed striatum during baseline, right after depolarization (early) and 16 s after depolarization (late); n = 8 and 13 neurons, mean ± s.e.m. Two-tailed Wilcoxon matched-pairs signed rant tests were performed: P = 0.0078 (upper left), 0.0234 (upper right), 0.0134 (bottom left) and 0.0266 (bottom right). **, $p < 0.01$; *, $p < 0.05$.

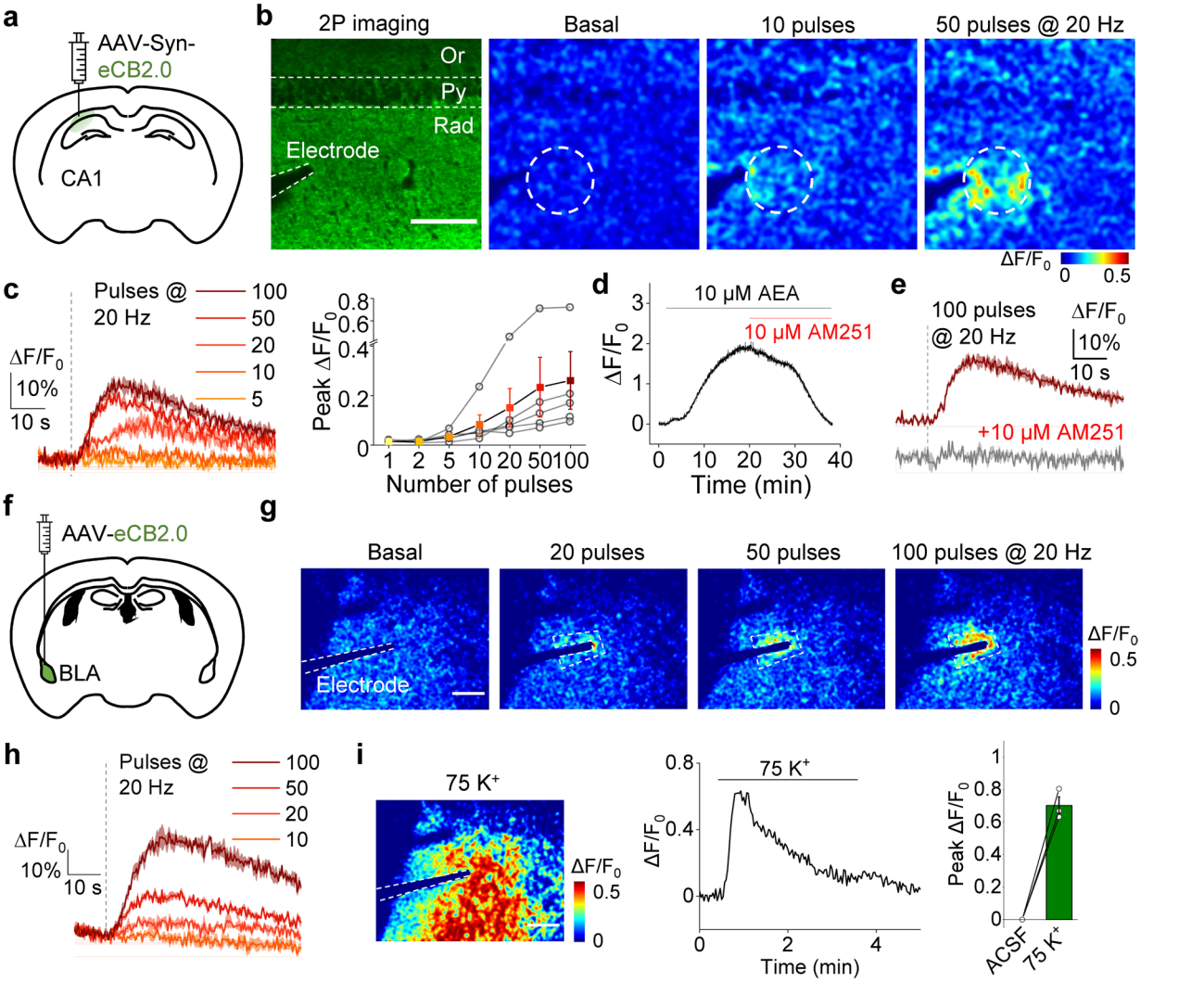

Extended Data Fig. 8 | Detection of eCB signals in acute hippocampal and BLA slices using 2 photon imaging. a, Schematic diagram depicting the strategy for virus injection in the hippocampal CA1 region, followed by the preparation of acute slices for electrical stimulation and 2-photon imaging. **b**, (Left) fluorescence image of eCB2.0 expressed in the hippocampal CA1 region, showing the position of the stimulating electrode. (Right) pseudocolor images showing the change in eCB2.0 fluorescence at baseline and after 10 or 50 pulses applied at 20 Hz. The dashed circle shows the ROI for quantification. Similar results were observed for 5 slices. Scale bar, 100 μm. **c**, Representative traces and summary of the peak change in eCB2.0 fluorescence evoked by electrical pulses applied at the indicated frequencies; n = 5 slices, mean ± s.e.m. **d**, Time course of the change in eCB2.0 fluorescence; where indicated, AEA and AM251 were applied. **e**, Representative traces of the change in eCB2.0 fluorescence evoked by electrical stimulation in the absence and presence of AM251. **f**, Schematic diagram depicting the strategy for virus injection in the BLA region, followed by the preparation of acute slices for electrical stimulation and 2-photon imaging. **g**, Pseudocolor images showing the change in eCB2.0 fluorescence after 20, 50 or 100 pulses applied at 20 Hz. Similar results were observed for 3 slices. Scale bar, 100 μm. **h**, Traces of eCB2.0 fluorescence evoked by electrical pulses applied at the indicated frequencies. **i**, Representative pseudocolor image, trace, and summary of peak change in eCB2.0 fluorescence upon 75 mM K^+ ACSF perfusion. Scale bar, 100 μm. n = 3 slices, mean ± s.e.m.

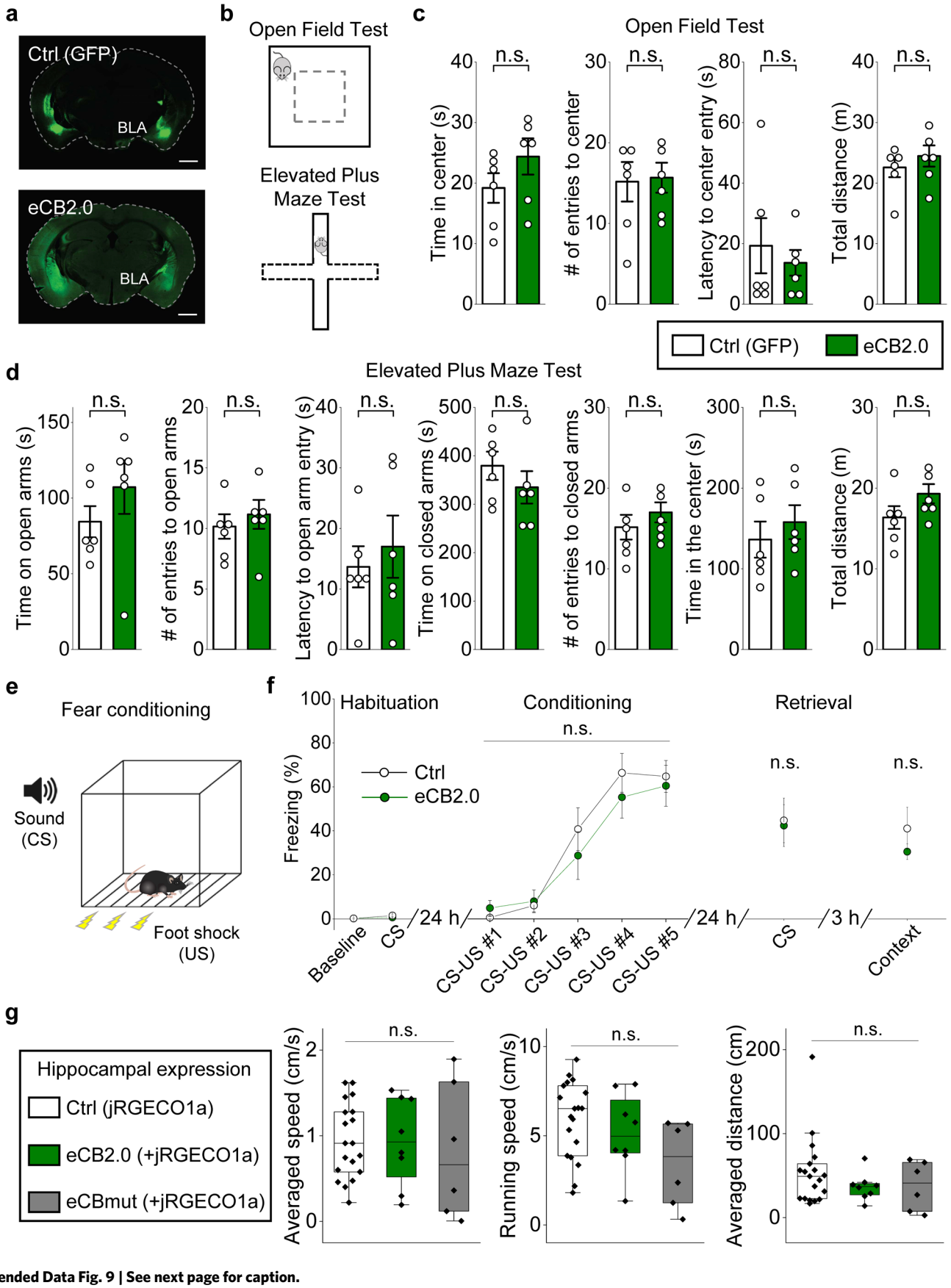

Extended Data Fig. 9 | See next page for caption.

Extended Data Fig. 9 | Expression of $GRAB_{eCB}$ sensors has minimal effect on animal behaviors. a, Fluorescence images of coronal slices prepared from mice expressing GFP or $GRAB_{eCB2.0}$ in BLA. Similar results were observed for 6 mice. Scale bar, 1 mm. **b**, Schematic diagrams showing the open field test (OFT) and the elevated plus maze test (EPMT). **c**, Quantification of behavioral parameters in the OFT. n = 6 mice, mean ± s.e.m. Two-tailed Student's t tests were performed: P = 0.2084, 0.8737, 0.5858 and 0.4464. **d**, Quantification of behavioral parameters in the EPMT. n = 6 mice, mean ± s.e.m. Two-tailed Student's t tests were performed: P = 0.2912, 0.5377, 0.6007, 0.3386, 0.3748, 0.4958 and 0.1411. **e**, Schematic diagram showing the fear conditioning test. **f**, Quantification of freezing behavior before, during and after conditioning. n = 6 mice, mean ± s.e.m. Two-way ANOVA test was performed: P = 0.3799 (between two animal groups during conditioning); two-tailed Student's t tests were performed: P = 0.3297 and 0.8669 (during retrieval). **g**, Quantification of averaged speed, running speed and averaged distance in control, eCB2.0 and eCBmut expressing mice; n = 19, 8 and 6 mice. Boxes show the first and third quartiles as well as the median (line), and the whiskers extend to the most extreme data point that is no more than 1.5× the interquartile range from the box. One-way ANOVA tests were performed: P = 0.9017, 0.0681 and 0.4197. n.s., not significant.

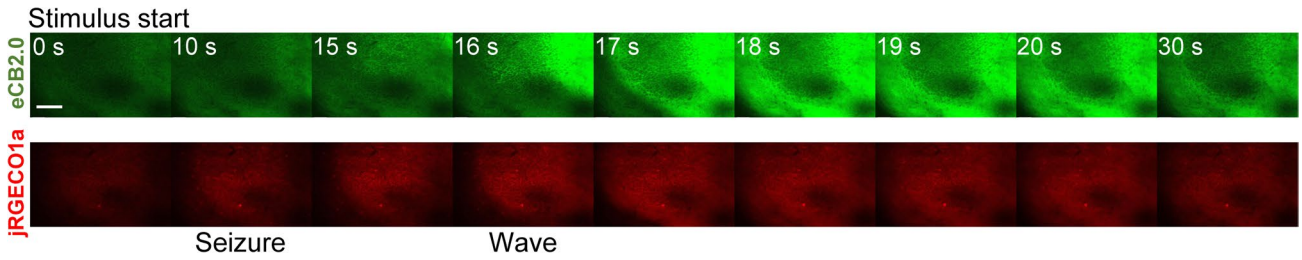

Extended Data Fig. 10 | eCB and Ca^{2+} waves in mouse hippocampal CA1 region during seizure activity. *In vivo* two-photon fluorescence images of eCB2.0 and jRGECO1a expressed in the mouse hippocampal CA1 region before and after stimulus evoked seizure activity. Frames were extracted from those shown in Supplementary Video 1. Seconds (s) after the stimulus are indicated. Similar results were observed for 6 mice. Scale bar, 100 μm.

nature research

Corresponding author(s): Yulong Li

Last updated by author(s): Aug 11, 2021

Reporting Summary

Nature Research wishes to improve the reproducibility of the work that we publish. This form provides structure for consistency and transparency in reporting. For further information on Nature Research policies, see our Editorial Policies and the Editorial Policy Checklist.

Statistics

For all statistical analyses, confirm that the following items are present in the figure legend, table legend, main text, or Methods section.

n/a	Confirmed	
☐	☒	The exact sample size (*n*) for each experimental group/condition, given as a discrete number and unit of measurement
☐	☒	A statement on whether measurements were taken from distinct samples or whether the same sample was measured repeatedly
☐	☒	The statistical test(s) used AND whether they are one- or two-sided *Only common tests should be described solely by name; describe more complex techniques in the Methods section.*
☒	☐	A description of all covariates tested
☐	☒	A description of any assumptions or corrections, such as tests of normality and adjustment for multiple comparisons
☐	☒	A full description of the statistical parameters including central tendency (e.g. means) or other basic estimates (e.g. regression coefficient) AND variation (e.g. standard deviation) or associated estimates of uncertainty (e.g. confidence intervals)
☐	☒	For null hypothesis testing, the test statistic (e.g. *F*, *t*, *r*) with confidence intervals, effect sizes, degrees of freedom and *P* value noted *Give P values as exact values whenever suitable.*
☒	☐	For Bayesian analysis, information on the choice of priors and Markov chain Monte Carlo settings
☒	☐	For hierarchical and complex designs, identification of the appropriate level for tests and full reporting of outcomes
☒	☐	Estimates of effect sizes (e.g. Cohen's *d*, Pearson's *r*), indicating how they were calculated

Our web collection on statistics for biologists contains articles on many of the points above.

Software and code

Policy information about availability of computer code

Data collection	The Harmony 4.9 software of Opera Phenix high-content screening system (PerkinElmer). The NIS-Element 4.51.00 software of Ti-E A1 confocal microscope (Nikon). The PHERAstar software Version 4.00 of PHERAstar FS plate reader (Berthold). The VICTOR 2030 Workstation software 4.0 of VICTOR 468 X5 multi-label plate reader (PerkinElmer). The XFLUOR4SAFIREII V 4.62n of Safire 2 plate reader (TECAN). The FV10-ASW software of FV1000MPE 2-photon microscope (Olympus). The Prairie View 5.5 software of Ultima Investigator 2P microscope (Bruker). The Clampex 10.0 software of Digidata 1550B digitizer (Molecular Devices). The Bonsai 2.3.1 and 2.6.2 of the photometry system (Neurophotometrics). The ZEN 2011 SP7 software of LSM780 and LSM710 confocal microscope (Zeiss).
Data analysis	ImageJ 1.53c (NIH), MATLAB R2018a (MathWorks), OriginPro 2020b (OriginLab), Python3.6 & 3.7, Prism 7.0 & 8.3 (GraphPad), SIMA Package (https://github.com/losonczylab/sima). Custom MATLAB and Arduino codes are available at https://github.com/hbhzshengao/dsi_events_analysis and https://github.com/hbhzshengao/2p_imaging_stim

For manuscripts utilizing custom algorithms or software that are central to the research but not yet described in published literature, software must be made available to editors and reviewers. We strongly encourage code deposition in a community repository (e.g. GitHub). See the Nature Research guidelines for submitting code & software for further information.

Data

Policy information about availability of data

All manuscripts must include a data availability statement. This statement should provide the following information, where applicable:

- Accession codes, unique identifiers, or web links for publicly available datasets
- A list of figures that have associated raw data
- A description of any restrictions on data availability

Plasmids for expressing the sensors used in this study and the sequences were available from Addgene (https://www.addgene.org/Yulong_Li/, #164604–164612).

Field-specific reporting

Please select the one below that is the best fit for your research. If you are not sure, read the appropriate sections before making your selection.

☒ Life sciences ☐ Behavioural & social sciences ☐ Ecological, evolutionary & environmental sciences

For a reference copy of the document with all sections, see nature.com/documents/nr-reporting-summary-flat.pdf

Life sciences study design

All studies must disclose on these points even when the disclosure is negative.

Sample size	No statistical methods were used to predetermine the sample size. Sample sizes are indicated for each experiment and were chosen based on similar studies. [1] Sun, F., Zhou, J., Dai, B., Qian, T., Zeng, J., Li, X., ... & Li, Y. (2020). Next-generation GRAB sensors for monitoring dopaminergic activity in vivo. Nature methods, 17(11), 1156-1166. [2] Inoue, M., Takeuchi, A., Manita, S., Horigane, S. I., Sakamoto, M., Kawakami, R., ... & Bito, H. (2019). Rational engineering of XCaMPs, a multicolor GECI suite for in vivo imaging of complex brain circuit dynamics. Cell, 177(5), 1346-1360. [3] Patriarchi, T., Mohebi, A., Sun, J., Marley, A., Liang, R., Dong, C., ... & Tian, L. (2020). An expanded palette of dopamine sensors for multiplex imaging in vivo. Nature methods, 17(11), 1147-1155. [4] Mohr, M. A., Bushey, D., Aggarwal, A., Marvin, J. S., Kim, J. J., Marquez, E. J., ... & Podgorski, K. (2020). jYCaMP: an optimized calcium indicator for two-photon imaging at fiber laser wavelengths. Nature methods, 17(7), 694-697. [5] Wan, J., Peng, W., Li, X., Qian, T., Song, K., Zeng, J., ... & Li, Y. (2021). A genetically encoded sensor for measuring serotonin dynamics. Nature Neuroscience, 24(5), 746-752.
Data exclusions	No data was excluded from the analysis.
Replication	All attempts at replication were successful. The replication number of each data is indicated in the legend of the corresponding figures.
Randomization	Cells and animals were randomly allocated into experimental groups.
Blinding	The investigators were not blinded to group allocation during data collection and analysis. The experimental conditions were obvious to the researchers and the analysis was performed objectively and not subjective to human bias.

Reporting for specific materials, systems and methods

We require information from authors about some types of materials, experimental systems and methods used in many studies. Here, indicate whether each material, system or method listed is relevant to your study. If you are not sure if a list item applies to your research, read the appropriate section before selecting a response.

Materials & experimental systems

n/a	Involved in the study
☐	☒ Antibodies
☐	☒ Eukaryotic cell lines
☒	☐ Palaeontology and archaeology
☐	☒ Animals and other organisms
☒	☐ Human research participants
☒	☐ Clinical data
☒	☐ Dual use research of concern

Methods

n/a	Involved in the study
☒	☐ ChIP-seq
☒	☐ Flow cytometry
☒	☐ MRI-based neuroimaging

Antibodies

Antibodies used	Chicken anti-GFP (1:1000, Aves, #GFP-1020) Rabbit anti-RFP (1:500, Rockland, #600-401-379)

Alexa Fluor 488 donkey anti-chicken (1:250, Jackson ImmunoResearch, #703-545-155)
Alexa Fluor 568 donkey anti-rabbit (1:250, Invitrogen, #A10042)

Validation

All antibodies were validated by the manufacturer and published research articles.

Chicken anti-GFP (Aves, #GFP-1020): https://www.aveslabs.com/products/green-fluorescent-protein-gfp-antibody?_pos=1&_sid=77fea58d3&_ss=r
Rabbit anti-RFP (Rockland, #600-401-379): https://rockland-inc.com/store/Antibodies-to-GFP-and-Antibodies-to-RFP-600-401-379-O4L_24299.aspx
Alexa Fluor 488 donkey anti-chicken (Jackson ImmunoResearch, #703-545-155): https://www.jacksonimmuno.com/catalog/products/703-545-155
Alexa Fluor 568 donkey anti-rabbit (Invitrogen, #A10042): https://www.thermofisher.com/cn/zh/antibody/product/Donkey-anti-Rabbit-IgG-H-L-Highly-Cross-Adsorbed-Secondary-Antibody-Polyclonal/A10042

Eukaryotic cell lines

Policy information about cell lines

Cell line source(s)	The HEK293T cell line was from ATCC (cat number CRL-3216). The modified HEK293 cell line used for Tango assay was a gift from Bryan L. Roth in University of North Carolina (Addgene, Kit #1000000068, see ref 45).
Authentication	The cell lines were authenticated based on the morphology under microscope and the analysis of the growth curve.
Mycoplasma contamination	The cell lines were not tested for mycoplasma contamination.
Commonly misidentified lines (See ICLAC register)	This study did not involve commonly misidentified lines.

Animals and other organisms

Policy information about studies involving animals; ARRIVE guidelines recommended for reporting animal research

Laboratory animals	Postnatal 0-day-old (P0) Sprague-Dawley rats (Beijing Vital River Laboratory), male and female. P42-P150 C57BL/6J mice (Beijing Vital River Laboratory and The Jackson Laboratory), male and female. P42-P150 CB1R-P2A-FlpO mice, male and female.
Wild animals	This study did not involve wild animals.
Field-collected samples	This study did not involve samples collected from the fields.
Ethics oversight	All experiment protocols were approved by the respective Laboratory Animal Care and Use Committees of Peking University, the National Institute on Alcohol Abuse and Alcoholism, the Cold Spring Harbor Laboratory, and Stanford University, and all studies were performed in accordance with the guidelines established by the US National Institutes of Health.

Note that full information on the approval of the study protocol must also be provided in the manuscript.